

Dark matter properties through cosmic history

Stéphane Ilic*

*CEICO, Institute of Physics of the Czech Academy of Sciences, Na Slovance 2, Praha 8, Czech Republic
Université PSL, Observatoire de Paris, Sorbonne Université, CNRS, LERMA, F-75014, Paris, France and
IRAP, Université de Toulouse, CNRS, CNES, UPS, Toulouse, France*

Michael Kopp†

*CEICO, Institute of Physics of the Czech Academy of Sciences, Na Slovance 2, Praha 8, Czech Republic and
Nordita, KTH Royal Institute of Technology and Stockholm University,
Hannes Alfvéns väg 12, SE-106 91 Stockholm, Sweden*

Constantinos Skordis‡

CEICO, Institute of Physics of the Czech Academy of Sciences, Na Slovance 2, Praha 8, Czech Republic

Daniel B. Thomas§

*Jodrell Bank Centre for Astrophysics, School of Physics & Astronomy,
The University of Manchester, Manchester M13 9PL, United Kingdom*

(Dated: September 10, 2021)

We perform the first test of dark matter (DM) stress-energy evolution through cosmic history, using cosmic microwave background measurements supplemented with baryon acoustic oscillation data and the Hubble Space Telescope key project data. We constrain the DM equation of state (EoS) in 8 redshift bins, and its sound speed and (shear) viscosity in 9 redshift bins, finding no convincing evidence for non- Λ CDM values in any of the redshift bins. Despite this enlarged parameter space, the sound speed and viscosity are constrained relatively well at late times (due to the inclusion of CMB lensing), whereas the EoS is most strongly constrained around recombination. These results constrain for the first time the level of “coldness” required of DM across various cosmological epochs at both the background and perturbative levels. We show that simultaneously allowing time dependence for both the EoS and sound speed parameters shifts the posterior of the DM abundance before recombination to a higher value, while keeping the present day DM abundance similar to the Λ CDM value. This shifts the posterior for the present day Hubble constant compared to Λ CDM, suggesting that DM with time-dependent parameters is well-suited to explore possible solutions to persistent tensions within the Λ CDM model. We perform a detailed comparison with our previous study involving a vanishing sound speed and viscosity using the same datasets in order to explain the physical mechanism behind these shifts.

I. INTRODUCTION

Galactic and cosmological observations indicate that if gravitational laws are dictated by general relativity, a large fraction of the nonrelativistic matter in our Universe is in the form of particles having negligible interaction with electromagnetism, baryons and themselves, and with negligible initial velocity dispersion. The existence of these particles has been demonstrated through their gravitational effects on the largest (galactic to cosmological) scales of the Universe. Collectively, they are successfully modeled as cold dark matter (CDM), a crucial component of the Λ CDM concordance model.

Although a plethora of concrete DM models have been proposed [10], dedicated direct and indirect astrophysical searches have yielded no convincing evidence for a DM particle so far. The strongest exclusion limits in the mass vs cross-section plane using direct detection through nuclear recoil

come from the Xenon1T experiment [5–8]. Meanwhile, possible signals of DM annihilation resulting in the positron excess detected by the Alpha Magnetic Spectrometer (AMS) instrument [2] are in conflict with the Planck collaboration [40] observations of the Cosmic Microwave Background (CMB) anisotropies, the latter being sensitive to energy injection in the intergalactic medium through such annihilations. Indeed, the AMS positron excess may be explained by conventional astrophysical mechanisms [3, 37].

This lack of nongravitational evidence necessitates further testing of the CDM paradigm. Taking a more agnostic approach with this in mind, we test possible departures from CDM using the phenomenologically motivated generalized dark matter (GDM) model [23]. GDM compactly parametrizes the DM properties encapsulated by pressure and viscosity using three parametric functions: the background equation of state (EoS) $w(a)$ of DM, sound speed $c_s^2(a, k)$ and the viscosity $c_{\text{vis}}^2(a, k)$, where a is the scale factor and k the wave number of the linearized GDM fluid fluctuations.

In [23] it was shown that the expansion history and consequently the CMB anisotropies angular power spectrum is particularly sensitive to these parameters. Moreover, when w is a constant, [23] uncovers a degeneracy between w and $\omega_g^{(0)}$, the dimensionless DM density today. An extensive investigation of the model was presented in [28] where its possible

* stephane.ilic@obspm.fr

† michael.kopp@su.se

‡ skordis@fzu.cz

§ daniel.thomas-2@manchester.ac.uk

connection to more fundamental theories was established, particularly to K -essence scalar fields, a rich internally coupled dark sector (e.g. dark matter coupled to dark radiation), thermodynamics and effective field theories. Furthermore, [28] analysed an exact solution of the perturbed Einstein equations in a flat GDM-dominated universe uncovering a degeneracy between a constant sound speed and constant viscosity. Specifically, the effective perturbative parameter relevant for the CMB is $c_s^2 + \frac{8}{15}c_{\text{vis}}^2$ and in order to break this degeneracy, different types of observations are necessary.

Constraints on constant GDM parameters were placed previously by [14, 31, 38, 49] using a variety of datasets. The latest constraints on constant GDM parameters were reported in [44] and [32] using CMB data from the Planck satellite setting a limit on constant $|w| \lesssim 10^{-3}$ and $c_s^2, c_{\text{vis}}^2 \lesssim 10^{-6}$. Significant improvements on the perturbative parameters c_s^2 and c_{vis}^2 were obtained in [32] and [43] through the inclusion of the late-time clustering data. Using late-time clustering data, however, is prone to introducing systematic modeling errors due to the nonlinearities inherent in the processing of these datasets. Thus, to test that the improvement in c_s^2 and c_{vis}^2 is robust, [43] designed a nonlinear extension of the GDM model based on the ‘‘warm and fuzzy’’ dark matter halo model, which incorporates certain nonlinear phenomena. Joint constraints on the sum of neutrino masses and constant GDM parameters were obtained in [30, 43]. A time-varying equation of state w was considered in [29] by piecewise parametrizing $w(a)$ in 8 redshift bins, while both c_s^2 and c_{vis}^2 were assumed to be zero. There, the most general time-evolution of the DM equation of state was tested, yet no evidence for DM properties beyond CDM was found. Interestingly, while data allow w to be fairly larger than zero in the late universe, between matter-radiation equality and CMB recombination $|w|$ is $\lesssim 10^{-3}$ and thus DM must behave very closely to CDM during that time [29].

Although a wealth of more constraining data exists, by sticking to observables pertaining to linear perturbations and Friedmann-Lemaître-Robertson-Walker (FLRW) background one reduces systematic uncertainties and modeling errors (on the nonlinear scales) to a minimum. This ensures that any potential detection of nonzero GDM parameters can be convincingly interpreted as a detection of DM properties. We refer however to [32, 43, 45] for potential applications to nonlinear scales.

In this article, we present the most exhaustive parameter search to date, allowing all three GDM parametric functions $w(a)$, $c_s^2(a)$ and $c_{\text{vis}}^2(a)$ to have a sufficiently general time dependence. This time dependence is modeled by binning $w(a)$ in 8 and c_s^2 and c_{vis}^2 in 9 scale factor bins, totalling 26 new parameters beyond CDM. We use the same datasets as our previous study which had a time-dependent $w(a)$ but zero $c_s^2(a)$ and $c_{\text{vis}}^2(a)$ [29]; this allows us to perform a detailed comparison of the effects of the new enlarged parameter space corresponding to $c_s^2(a)$ and $c_{\text{vis}}^2(a)$ with respect to [29].

The structure of the article is as follows. We give a brief summary of the GDM model, describe our binning strategy and present the various models and submodels that we study in Sec. II. In Sec. III we present our methodology, including numerical solutions, the datasets and sampling method used

which allowed exploration of the very high-dimensional parameter space and a discussion of our choice of priors. Our results are presented in Sec. IV, specifically constraints on the DM EoS and abundance, constraints on the sound speed and viscosity, degeneracies and a special submodel where all three functions are set to be equal. We discuss the physical aspects and implications of our results in Sec. V, particularly, the tight constraint of the GDM comoving density perturbation in the early universe and how some GDM models may alleviate the Hubble tension. We conclude in Sec. VI.

The reader may find useful the three appendices. In Appendix A we derive an expression for the growth index in a Λw DM (i.e. GDM with constant EoS and zero sound speed and viscosity) and discuss the Integrated Sachs-Wolfe (ISW) effect. We describe our publicly available suite of codes used here for sampling the parameter space and visualizing the results in Appendix B. A complete list of constraints for various choices of datasets, parametrization choices and priors as well as correlation matrices can be found in Appendix C.

II. THE MODEL

A. Evolution equations

We consider a flat FLRW background with only scalar perturbations, see [28] for more details and notation. The GDM background density $\bar{\rho}_g$ and pressure \bar{P}_g evolve according to the conservation law

$$\dot{\bar{\rho}}_g = -3H(1+w)\bar{\rho}_g, \quad \dot{\bar{P}}_g = w\bar{\rho}_g, \quad (2.1)$$

where $H = \frac{\dot{a}}{a}$ is the Hubble parameter, satisfying the Friedmann equation, and the overdot denotes derivatives with respect to cosmic time t . The parametric function $w(a)$ can be freely specified and contains with $w = 0$ the CDM model ($\bar{\rho}_g = \bar{\rho}_c$). The GDM model has two further free parametric functions, the speed of sound, $c_s^2(a, k)$, and the (shear) viscosity, $c_{\text{vis}}^2(a, k)$, both of which are zero in the case of CDM.

The synchronous gauge metric perturbed around a flat FLRW background is given by

$$ds^2 = -dt^2 + a^2 \left[\left(1 + \frac{1}{3}h\right) \delta_{ij} + (\vec{\nabla}_i \vec{\nabla}_j - \frac{1}{3}\gamma_{ij} \vec{\nabla}^2) \nu \right] dx^i dx^j, \quad (2.2)$$

where $\vec{\nabla}_i$ is the covariant derivative compatible with the Euclidean metric γ_{ij} and only scalar modes (in this gauge h and ν) are considered.

Switching to k -space, the general GDM fluid equations for the density contrast δ_g and velocity perturbation θ_g are given by

$$\dot{\delta}_g = 3H(w\delta_g - \Pi_g) - (1+w) \left[\frac{k^2}{a} \theta_g + \frac{1}{2}\dot{h} \right] \quad (2.3a)$$

$$a\dot{\theta}_g = -(1 - 3c_a^2)aH\theta_g + \frac{\Pi_g}{1+w} - \frac{2}{3}k^2\Sigma_g. \quad (2.3b)$$

with $c_a^2 = \dot{P}_g/\dot{\rho}_g$. While the above equations are generically valid for any conserved fluid, the following special choice of closure equations, defines the GDM model [23]

$$\Pi_g = c_s^2 \delta_g + 3(1+w)(c_s^2 - c_a^2) a H \theta_g \quad (2.3c)$$

$$\dot{\Sigma}_g = -3H\Sigma_g + \frac{4}{1+w} c_{\text{vis}}^2 \left(\frac{\theta_g}{a} - \frac{1}{2} \dot{v} \right). \quad (2.3d)$$

The first equation is a perturbative EoS for the pressure perturbation $\Pi_g \equiv (P_g - \bar{P}_g)/\bar{\rho}_g$ and the second equation is an evolution equation for the scalar part Σ_g of the traceless part of the GDM stress tensor T_{gj}^i . We refer the interested reader to [28] for further discussions of the theoretical motivation, physical interpretation and notation.

The EoS w is expected to be uncorrelated with the two perturbative parameters c_s^2 and c_{vis}^2 during the era of matter domination, as shown in [44]. However, as we show below, these parameters become correlated during the era of radiation domination, when adiabatic initial conditions are considered.

B. Smooth bin parametrization

In order to constrain the three purely time-dependent GDM parametric functions $w(a)$, $c_s^2(a)$ and $c_{\text{vis}}^2(a)$ in a way that is sufficiently general but still feasible, we restricted the variation of these functions to $N = 9$ scale factor bins. As our goal is to explore the allowed behavior of dark matter with as few restrictions as possible, having fewer bins would unnecessarily restrict the phenomenological freedom of the model.

The bin edges were chosen to be

$$\begin{aligned} \tilde{a}_0 &= 1 \\ \tilde{a}_{1 \leq i \leq N-1} &= 10^{-i \Delta_{\ln a}} \quad \text{with } \Delta_{\ln a} = 0.5 \\ \tilde{a}_N &= 0 \end{aligned} \quad (2.4)$$

so that $f(a)$ (here denoting any of w , c_s^2 , c_{vis}^2) has piecewise constant values between them, that is,

$$f(a) = \sum_{i=0}^{N-1} f_i \Theta(a - \tilde{a}_{i+1}) \Theta(\tilde{a}_i - a), \quad (2.5)$$

with the f_i coefficients comprising N free parameters and Θ is the Heaviside step function. In the case of the $w(a)$ function, the discontinuity at the bin edges $\tilde{a}_{1 \leq i \leq N-1}$ implies $c_{a,i}^2(\tilde{a}_i) = \pm\infty$ for the adiabatic sound speed. In order to test whether our conclusions depend on this discontinuity, we regularized the transitions by a lognormal smoothing of Eq. (2.5) with width $\sigma_{\ln a}$ (and assuming $\sigma_{\ln a} \ll \Delta_{\ln a}$), leading to

$$\begin{aligned} f(a) &= \sum_{i=0}^{N-2} \tilde{f}_i(a) \Theta(a - a_{i+1}) \Theta(a_i - a) \\ \tilde{f}_i(a) &= \frac{f_i - f_{i+1}}{2} \operatorname{erf}\left(\frac{\ln(a/\tilde{a}_{i+1})}{\sigma_{\ln a}}\right) + \frac{f_i + f_{i+1}}{2}, \end{aligned} \quad (2.6)$$

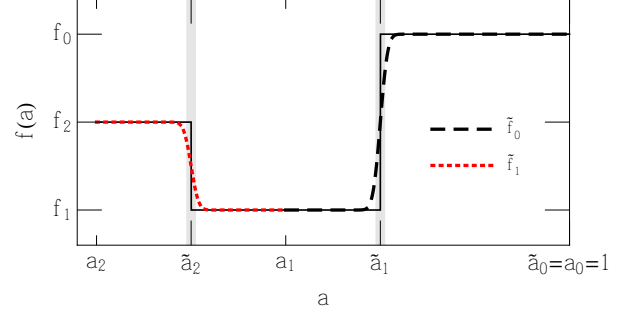


FIG. 1. Dashed lines show the first two components of the sum in Eq. (2.6) in an arbitrary case where $f_1 < f_2 < f_0$. The black thin line shows the first three components of the sum in Eq. (2.5). The width of the grey bands corresponds to $\sigma_{\ln a}$.

with corresponding logarithmic bin centers¹

$$\begin{aligned} a_0 &= 1 \\ a_{1 \leq i \leq N-2} &= \sqrt{\tilde{a}_i \tilde{a}_{i+1}} \\ a_{N-1} &= 10^{-\Delta_{\ln a}} \tilde{a}_{N-1}. \end{aligned} \quad (2.7)$$

We set $\sigma_{\ln a} = 0.1 \Delta_{\ln a}$, a sufficiently small choice in order to avoid introducing unwanted physical effects, but sufficiently wide to study potential differences to setting $\sigma_a = 0$ corresponding to Eq. (2.5). Both choices produced the same constraints. See Fig. 1 for a visual representation of Eq. (2.6).

C. Definition of models and submodels

We list here the different types of (sub)models that we used for our study of GDM.

a. Model “var-wc”: The most general GDM model based on our parametrization with all 26 GDM parameters included is denoted by “var-wc”. In addition to this model, we consider and study separately the three nested submodels below. We note that as discussed in [29], a degeneracy between w and Λ is present in the late universe. With this in mind, the last two w -bins were merged by setting $w_0 = w_1$ in this model, as well as its submodel *var-w*.

b. Submodel “var-w”: The submodel obtained by setting $c_s^2 = c_{\text{vis}}^2 = 0$ while keeping the 8 w_i s free, is denoted by “var-w” and has been previously studied in [29]. It describes a GDM fluid that only modifies the background evolution of the Universe, but maintains the geodesic motion of GDM fluid elements. We include this model here for reference purposes, as the present paper is a direct generalization and logical continuation of [29]. The inclusion of this model allows us to

¹ For convenience we defined the bin centers for the first and last bin separately. Any definition of bin center is acceptable if it is several multiples of $\sigma_{\ln a}$ away from the transition times $\ln \tilde{a}_{1 \leq i \leq N-2}$.

Model	Additional parameters	Restrictions	No. of additional parameters
<i>var-wc</i>	$w_i, c_{s,i}^2, c_{\text{vis},i}^2$	$w_0 = w_1$	26 (8 + 2 × 9)
<i>var-w</i>	w_i	$w_0 = w_1$ $c_s^2 = c_{\text{vis}}^2 = 0$	8 (9-1)
<i>var-c</i>	$c_{s,i}^2, c_{\text{vis},i}^2$	$w = 0$	18 (2 × 9)
<i>var-w=c</i>	$c_{s,i}^2$	$w = c_s^2 = c_{\text{vis}}^2$	9 (1 × 9)

TABLE I. List of the GDM models studied in this work.

check to what extent the previously obtained *var-w* constraints are recovered within the encompassing *var-wc* model after marginalization over the 18 additional $c_{s,i}^2$ and $c_{\text{vis},i}^2$ parameters. The bins w_0 and w_1 were once again joined together.

c. Submodel “var-c”: Using the same reasoning for studying the *var-w* model, we also study the complementary submodel “*var-c*” defined by $w = 0$ with all of the 18 $c_{s,i}^2$ and $c_{\text{vis},i}^2$ parameters left free.

d. Submodel “var-w=c”: Finally, we also consider the submodel with the restriction $w_i = c_{s,i}^2 = c_{\text{vis},i}^2$. This model is interesting due to its close relation with a number of well-motivated collisionless DM scenarios. Two examples are the case of warm DM and the case of CDM when the effects of unresolved nonlinear small-scale physics is incorporated using the effective field theory of large-scale structure [EFTofLSS, 9, 15, 16, 19]. In this case we let w_0 and w_1 be mutually independent since late universe constraints on w are driven by the c_s^2 and c_{vis}^2 functions, as we explain in Sec. IV D. Table I shows a summary of all GDM models considered in this paper.

It is also convenient to define a dimensionless scaled GDM density

$$\omega_g \equiv a^3 \bar{\rho}_g \frac{8\pi G}{3 \times (100 \text{ km/s/Mpc})^2}, \quad (2.8)$$

in order to facilitate interpreting constraints on w_i . When $w = 0$, ω_g is equal to the conventional (constant) dimensionless CDM density ω_c . The function ω_g is in general time dependent, however, fully determined by the $N + 1$ parameters $\omega_g^{(0)}, w_i$. We use the notation $\omega_g^{(i)} = \omega_g(a_i)$ and similarly for other functions with subscripts, so that the present day DM abundance is $\omega_g^{(0)} = \omega_g(a_0)$. Functions without subscript we write instead as $w_i = w(a_i)$.

III. METHODOLOGY

A. Numerical solutions

In order to perform our analysis we implemented the GDM fluid equations (2.1) and (2.3) in the Cosmic Linear Anisotropy Solving System (CLASS) code [33]. CLASS numerically solves the Boltzmann equation for each relevant component coupled to the Einstein equations and calculates the CMB and matter power spectra given a set of model parameters. Our modification of the CLASS code adds an additional GDM component based on the dark energy fluid (with

free equation of state and sound speed) implemented by the original authors [34], which we further improved to allow for nonzero viscosity.

Our modification of CLASS makes it easy to define as many bins as necessary for all three GDM functions $\{w, c_s^2, c_{\text{vis}}^2\}$ through the standard CLASS interface and to set the amplitudes for each of these functions in each bin. Following this work, our code is made publicly available² with instructions on how to use it.

We also independently modified a different Boltzmann code [DASH, 25] to include the full GDM parametrization. We performed a full comparison between the codes in the case of constant GDM parameters, including the background evolution, perturbation evolution, the CMB angular power spectra, matter power spectrum and lensing potential. The numerical difference of the two codes in the case of the GDM model is similar to the corresponding difference in the case of Λ CDM, within $\sim 0.1\%$. This level of agreement holds for all quantities in both the synchronous gauge and the conformal Newtonian gauges.

B. Datasets and sampling technique

Our constraints are obtained using the same datasets as in [29]. Specifically we used the Planck 2015 data release [41] of the CMB anisotropies power spectra, composed of the low- ℓ T/E/B likelihood and the full TT/TE/EE high- ℓ likelihood with its complete set of nuisance parameters. The combination of these likelihoods is thereafter referred to as Planck power spectra (PPS). We also selectively added the HST key project prior on H_0 [42], BAO measurements from the 6dF Galaxy Survey [11] and the Baryon Oscillation Spectroscopic Survey Sloan Digital Sky Survey [4], and the Planck 2015 CMB lensing likelihood (respectively referred to as HST, BAO and Lens). Although more recent cosmological datasets are available [see e.g 40], keeping to the ones mentioned above allows us to perform a robust comparison with our previous work [29] where $c_s^2 = c_{\text{vis}}^2 = 0$ in order to elucidate the effects of the new enlarged parameter space.

Our total cosmological parameter set (not including the Planck likelihood nuisance parameters)

$$(\omega_b, \omega_g^{(0)}, H_0, n_s, \tau, \ln 10^{10} A_s, w_i, c_{s,i}^2, c_{\text{vis},i}^2) \quad (3.1)$$

consists of 6 Λ CDM parameters and 8 values w_i , 9 values $c_{s,i}^2$ and 9 values $c_{\text{vis},i}^2$. We assumed adiabatic initial conditions, described in [28].

We investigated the constraints on our selection of GDM (sub)models coming from our choice of datasets using a standard Markov Chain Monte Carlo (MCMC) approach. For this purpose we used ECLAIR, a publicly available³ suite of codes that uses the numerical output from CLASS, combined with

² https://github.com/s-ilic/gdm_class_public

³ <https://github.com/s-ilic/ECLAIR>

likelihoods of state-of-the-art datasets, and efficient sampling methods.

To sample the parameter space we used the Goodman-Wear affine-invariant ensemble sampling technique [21] via our ECLAIR framework which internally uses the technique’s Python implementation `emcee` [20]. The convergence of the MCMC chains was assessed using graphical and numerical tools included in the ECLAIR code package (see Appendix B for more details). The ECLAIR suite was also used to find the point in parameter space corresponding to the maximum likelihood of each model. The resulting chains were used to determine the marginalized posterior distributions of the parameters using the publicly available code `getdist` [35].

C. Priors

We set uniform priors as specified in Table II unless otherwise stated. We used the same priors on Planck nuisance parameters and the same neutrino treatment as in [29, 44]. The helium fraction was set to $Y_{\text{He}} = 0.24667$ [39]. We have checked that letting Y_{He} be an additional free parameter in our MCMC analysis does not affect our results and conclusions.

We set flat priors on standard cosmological parameters as well as the GDM parameters (see Table II).⁴ The choice of priors is always a sensitive issue in any type of Bayesian analysis. This is particularly true in our case, as many of our parameters have a physical lower bound – namely sound speed and viscosity need to be positive at all times. These bounds form a (multidimensional) “corner” which due to volume effects becomes highly disfavored during the MCMC exploration regardless of whether the data favor this region of the parameter space or not. This situation is particularly problematic in our case because this corner corresponds to the standard CDM paradigm (zero sound speed and viscosity) and could be, thus, erroneously excluded by our MCMC analysis. Moreover, due to correlations with all other cosmological parameters, the corresponding marginalized posteriors of the set of sound speed and viscosity parameters might also be affected.

In order to alleviate these effects and test the sensitivity of our constraints on our choice of priors, we also used nonflat priors for $c_{s,i}^2$ and $c_{\text{vis},i}^2$, keeping the priors on the other parameters unchanged. For this test, we used flat priors on the combinations

$$\begin{aligned} c_{+,i}^2 &\equiv c_{s,i}^2 + \frac{8}{15}c_{\text{vis},i}^2 \\ b_i &\equiv \frac{15c_{s,i}^2}{15c_{s,i}^2 + 8c_{\text{vis},i}^2} \end{aligned} \quad (3.2)$$

which results in nonflat priors for the $c_{s,i}^2$ and $c_{\text{vis},i}^2$ set of parameters since the measure transforms as

$$dc_{+,i}^2 db_i \propto \frac{dc_{s,i}^2 dc_{\text{vis},i}^2}{c_{+,i}^2}. \quad (3.3)$$

⁴ Throughout H_0 is in units of $\text{km s}^{-1} \text{Mpc}^{-1}$, and H_{eq}^{-1} and r_s^{drag} are in units of Mpc.

Parameter	Prior	Model
ω_b	[0., 1.]	all
$\omega_g^{(0)}$	[0., 1.]	all
H_0	[45., 90.]	all
$\ln(10^{10} A_s)$	[2., 4.]	all
n_s	[0.8, 1.2]	all
τ_{reio}	[0.01, 0.8]	all
w_i	[-1., 1]	var-w & var-wc
$c_{s,i}^2$	[0., 1.]	var-c & var-wc
$c_{\text{vis},i}^2$	[0., 1.]	var-c & var-wc

TABLE II. List of free cosmological parameters and priors.

We refer to these priors as “nonflat priors” when discussing the *var-wc* and *var-c* models.

These priors are physically motivated. During GDM domination the scale below which the gravitational potential decays is determined by $c_+ \eta$, where η is the conformal time [44]. The b parameter interpolates linearly between the two extremes of 100% sound speed or 100% viscosity contribution to c_+^2 . After the leading-order effect determined by c_+ sets in, the quantity $b = c_s^2/c_+^2$ results in subleading effects, given a fixed c_+^2 . Thus, it seems natural to assume flat priors on the $\{c_{+,i}^2, b_i\}$ set of parameters rather than on $c_{s,i}^2$ and $c_{\text{vis},i}^2$. Flat priors on c_+^2 and b translate then into priors on c_s^2 and c_{vis}^2 which peak at the values $c_s^2 = 0$ and $c_{\text{vis}}^2 = 0$, as implied by (3.3). Hence, we call these “nonflat priors”. When viewed in the c_s^2 - c_{vis}^2 plane, these nonflat priors give more weight to the CDM “corner” $c_s^2 = c_{\text{vis}}^2 = 0$ and thus are expected to lead to tighter constraints on c_s^2 and c_{vis}^2 .

IV. RESULTS

The main results of this work are (i) the constraints on the time dependence of the DM EoS $w(a)$ and abundance $\omega_g(a)$ from the *var-wc* model shown in Figs. 2 and 3 and (ii) the constraints on $c_s^2(a)$ and $c_{\text{vis}}^2(a)$ from *var-wc* and *var-c* shown in Fig. 4. For comparison, we also show the constraints on the *var-w* model discussed previously in [29].

Interestingly, comparing the best (i.e. lowest) χ^2 for the three GDM models to the corresponding χ^2 in ΛCDM , i.e. $\Delta\chi_{\text{GDM}}^2 \equiv \chi_{\Lambda\text{CDM}}^2 - \chi_{\text{GDM}}^2$, we find $\Delta\chi_{\text{var-wc}}^2 \simeq \Delta\chi_{\text{var-w}}^2 \simeq 8$ and $\Delta\chi_{\text{var-c}}^2 \simeq 0$. To elaborate, adding the 8 new w_i parameters improves the fit only marginally ($\Delta\chi^2 \simeq 8$). However, adding the 18 new parameters for sound speed and viscosity yields virtually no improvement to the fit whether added by themselves (*var-c* submodel) or within the full *var-wc* model. We note that since we do not expect our numerous new GDM parameters to be physical, it makes little sense to apply model selection criteria to our GDM models.

The list of the 68% and 95% credible regions of the 1D-posteriors as well as best-fit values of the *var-wc* and *var-c* models for all parameters and datasets may be found in Appendix C. In the following sections we discuss the constraints in detail.

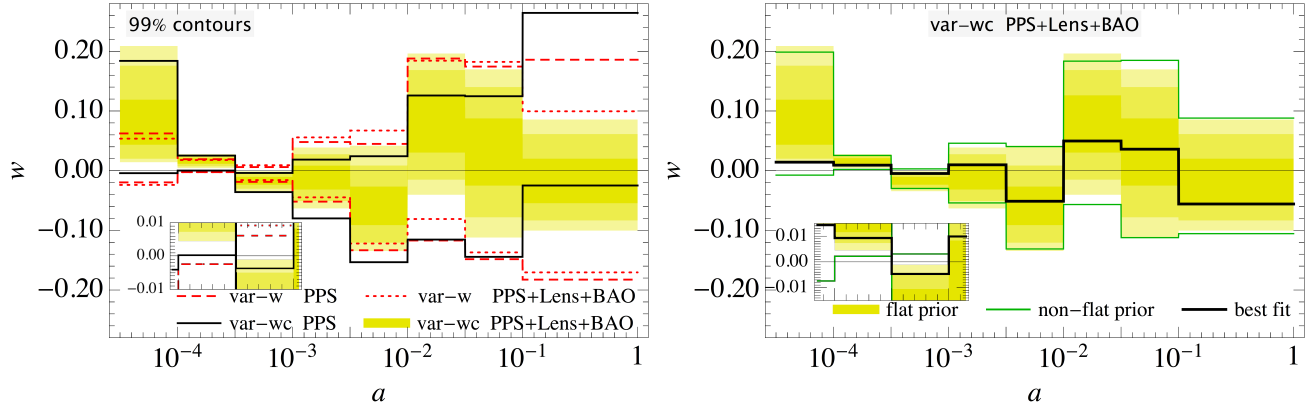


FIG. 2. Shown are the 99% credible regions on the w_i parameters parametrized the EoS of DM. The large ticks on the a -axis specify the bin boundaries. The line styles correspond to different datasets and models specified in the legend. The insets zoom into the region enclosing $w = 0$ and have the same ticks on the a -axis. *Left*: We show the credible regions for the *var-wc* and *var-w* models when PPS and PPS+Lens+BAO dataset combinations are used. In the *var-wc* model, the Λ CDM model (thin black solid line $w = 0$) lies outside the 99% credible region for bins 8, 7 and 6 when PPS+Lens+BAO (yellow shaded regions; darker shades correspond to 95% and 68%) was used while when PPS (black full line) was used only bin 7 is marginally inconsistent with Λ CDM. The *var-w* model (red dashed and red dotted) is, however, consistent with Λ CDM for all datasets. *Right*: Comparing flat and nonflat priors in the *var-wc* model with the dataset PPS+Lens+BAO combination. The yellow shaded region corresponds to 99% (darker shades as on the left) credible regions. For the nonflat priors (green full line) only bin 7 does not include $w = 0$. The best fit model is shown as thick black line which deviates significantly from the mean in the early universe. In bin 8 (leftmost bin), the best fit model lies at the lower edge of the lower 99% credible region of the flat prior case (lower boundary of the yellow region), while it is well contained for the nonflat prior (full green).

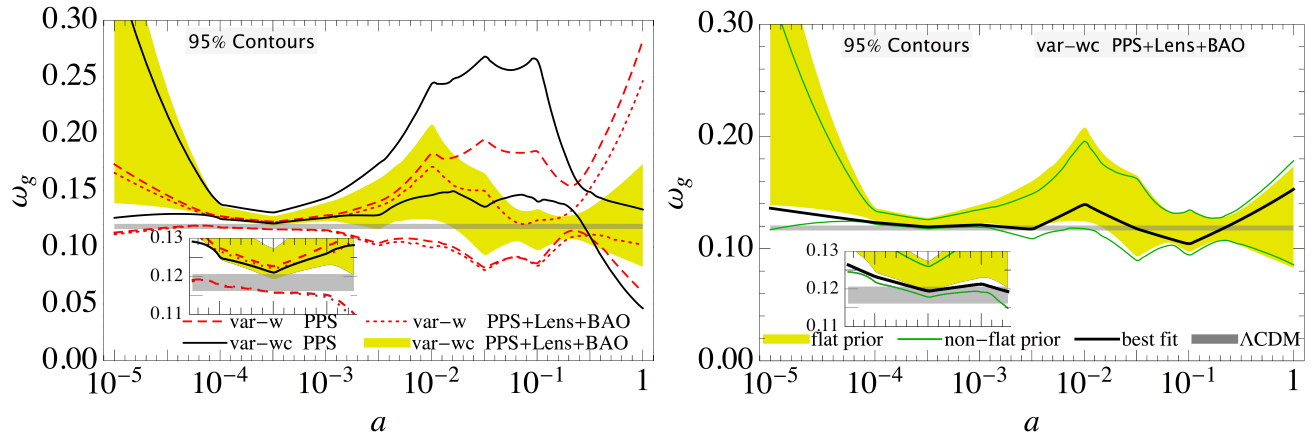


FIG. 3. Shown are the 95% credible regions on the scaled DM abundance $\omega_g(a)$ with same color scheme as in Fig. 2. The grey band corresponds to the Λ CDM constraint for PPS+Lens+BAO.

A. Constraints on DM EoS and abundance: *var-wc* and *var-w*

1. Equation of state, $w(a)$

In Fig. 2 we show constraints on w contrasting several models (*var-w*, *var-wc*), datasets (PPS, PPS+Lens+BAO) and priors (flat and nonflat priors for sound speed and viscosity). Quite interestingly, we observe on the left panel and in the case of the *var-wc* model that Λ CDM lies outside the 99% credible region in the earliest universe bins ($i = 8, 7$, and 6) when the PPS+Lens+BAO dataset was used (yellow shaded

region). In contrast, when the same dataset was used to constrain the *var-w* model (e.g. with $c_s^2 = c_{\text{vis}}^2 = 0$) the credible regions of w_i are consistent with zero, and thus Λ CDM, in all of the bins (red dotted lines).

Consider now the right panel of Fig. 2 which singles out the *var-wc* model constrained with the PPS+Lens+BAO dataset combination – the most discrepant with Λ CDM – on the left panel. There we display the impact of using different priors on constraining this model: the flat priors on $c_{s,i}^2$ and $c_{\text{vis},i}^2$ versus the nonflat priors on the same parameters, the latter corresponding to flat priors on the parameters defined by (3.2). We see that using the nonflat priors makes the early universe cred-

ible regions shift significantly (green lines) so that all bins, except the 7th bin, become consistent with Λ CDM, although even the 7th bin's tension with Λ CDM is reduced to $\sim 3\sigma$. Furthermore, the best fit model lies close to Λ CDM in bins 6, 7 and 8 and so we cannot decisively claim any nonzero detection of w .

We consider now the *var-wc* versus the *var-w* model. Even in the late universe (rightmost) bins where the priors on $c_{s,i}^2$ and $c_{\text{vis},i}^2$ do not have profound impact (see right panel of Fig. 2), marginalization over c_s^2 and c_{vis}^2 in the *var-wc* model shifts the credible regions significantly (see the left panel of Fig. 2 and compare the red dotted lines with the yellow shaded region). These differences between the two models at late times are present also when the PPS dataset is used (contrasting red lines versus black dashed line on the left of Fig. 2). Clearly then, marginalization over c_s^2 and c_{vis}^2 in the *var-wc* model does not lead to the same constraints on w as simply setting $c_s^2 = c_{\text{vis}}^2 = 0$ (the *var-w* model). We discuss in more detail the origin of the differences between these two models in the late and early universe in Sec. V.

We find strongest constraints on w between a_6 and a_5 which enclose the matter-radiation equality $a_{\text{eq}} \approx 3 \times 10^{-4}$. In other bins the constraints on w weaken significantly. Adding the BAO or HST dataset has only a minor effect on *var-w* constraints and only tightens limits in the rightmost bin. Contrary to the case of the *const-w* model [where w is a constant throughout the evolution of the universe and c_s^2 and c_{vis}^2 are zero, 44], and the *var-w* model [29], adding CMB lensing in the *var-wc* model significantly shifts the constraints on w_8 away from Λ CDM. This is seen by comparing the yellow shaded with the solid black region in the left panel of Fig. 2. The reasons for this will be discussed in detail in Sec. V.

2. Dark matter abundance, $\omega_g(a)$

The derived parameter $\omega_g(a)$, shown in Fig. 3, provides a better intuition on the meaning of the constraints on w_i . The $\omega_g(a)$ parameter is constructed via analytically integrating (2.1) given a set of w_i and $\omega_g^{(0)}$. Figure 3 shows the same model and dataset combinations as Fig. 2. Paradoxically, having free sound speed and viscosity in the *var-wc* model restricts the posterior of $\omega_g^{(0)}$. This explains why after marginalizing over c_s^2 and c_{vis}^2 , the w_0 constraints improve compared to the *var-w* submodel. The improvement of the $\omega_g^{(0)}$ posterior in *var-wc* compared to *var-w* is discussed in Sec. V.

The most striking difference with the $w(a)$ -constraints is the persistent offset of ω_g between the *var-wc* and Λ CDM models in the early universe, i.e. for all $a < 10^{-2}$. During the best-constrained period in a , around the time of matter-radiation equality $a_{\text{eq}} \approx 3 \times 10^{-4}$, we found $\omega_g^{\text{eq}} = 0.1236_{-0.0041}^{+0.0044}$ for the 95% credible interval in the case of the *var-wc* model when the PPS+Lens+BAO dataset combination was used. For comparison, we obtain $\omega_c^{\text{eq}} = 0.1184_{-0.0020}^{+0.0021}$ in Λ CDM with the same dataset combination. The same offset is present when only the PPS dataset is used, as seen in the inset of the left panel of Fig. 3 (black lines), whereas the *var-w* model (red dotted line)

leads to virtually the same value for ω_g^{eq} as Λ CDM for both dataset combinations.

The right panel in Fig. 3 focuses on the impact of priors on c_s^2 and c_{vis}^2 . The green lines display the 95% credible regions obtained when using nonflat priors on c_s^2 and c_{vis}^2 that give more weight to Λ CDM, see (3.2). We see that the flat prior credible region (yellow shaded) is very similar to the nonflat prior region (green lines), suggesting that the offset of ω_g in the early universe is not caused by the choice of priors. The black line shows the best fit model obtained through maximization of the log-likelihood. The best fit model, which does not depend on priors, also stays above the Λ CDM 95% credible region (grey band), favoring higher values of ω_g in the pre-recombination era.

B. Constraints on sound speed and viscosity: *var-wc* and *var-c*

1. Constraints on c_s^2 and c_{vis}^2

We now turn to the constraints on the perturbative GDM parameters $c_{s,i}^2$ and $c_{\text{vis},i}^2$ with $0 \leq i \leq 9$. In the upper panel of Fig. 4 we compare the *var-wc* and *var-c* models (for which $w = 0$) for each of the dataset combinations, PPS and PPS+Lens+BAO. We also display the constraints on constant c_s^2 and c_{vis}^2 , labeled as “const”, found previously in [44] using the same respective dataset combinations (dashed grey and dot-dashed grey lines). We see from the upper panel of Fig. 4 that CMB alone (PPS) constrains the $c_{s,i}^2$ and $c_{\text{vis},i}^2$ in all redshift bins. The best constraints, nearly as good as for the constant parameter case (“const”), are achieved in the bin $i = 1$ for which $0.1 < a < 10^{-0.5}$ (redshift $2.2 \lesssim z < 9$), where the gravitational lensing of the CMB is most efficient [see e.g. 36]. This secondary anisotropy, which smoothes the amplitude of the peaks and troughs of the CMB spectra without changing their location, most strongly constrains the perturbative GDM parameters.

The earliest parameters $c_{s,8}^2$ and $c_{\text{vis},8}^2$ are mostly constrained, however, through the primary CMB anisotropies. This may be inferred by comparing the yellow and black regions of the top two panels of Fig. 4, or the PPS and PPS+Lens columns (blue numbers) of Table III (see Appendix C) which indicates that CMB lensing (Lens dataset) indeed improves all constraints by a factor 2-4 except for $c_{s,8}^2$ and $c_{\text{vis},8}^2$. Note that this is a much bigger improvement than for the constant parameters, where BAO+Lens reduced the upper limits by a factor less than 2 [44].

The effect of using different priors, flat versus nonflat (see Sec. III C), is depicted in the lower panel of Fig. 4. There, only the PPS+Lens+BAO dataset combination is chosen. We also show the best-fit *var-c* and *var-wc* models which are prior-independent. Since the nonflat prior favors the Λ CDM corner in the c_s^2 - c_{vis}^2 plane, we expect tighter constraints in the nonflat prior case. This is what is observed in the lower panels of in

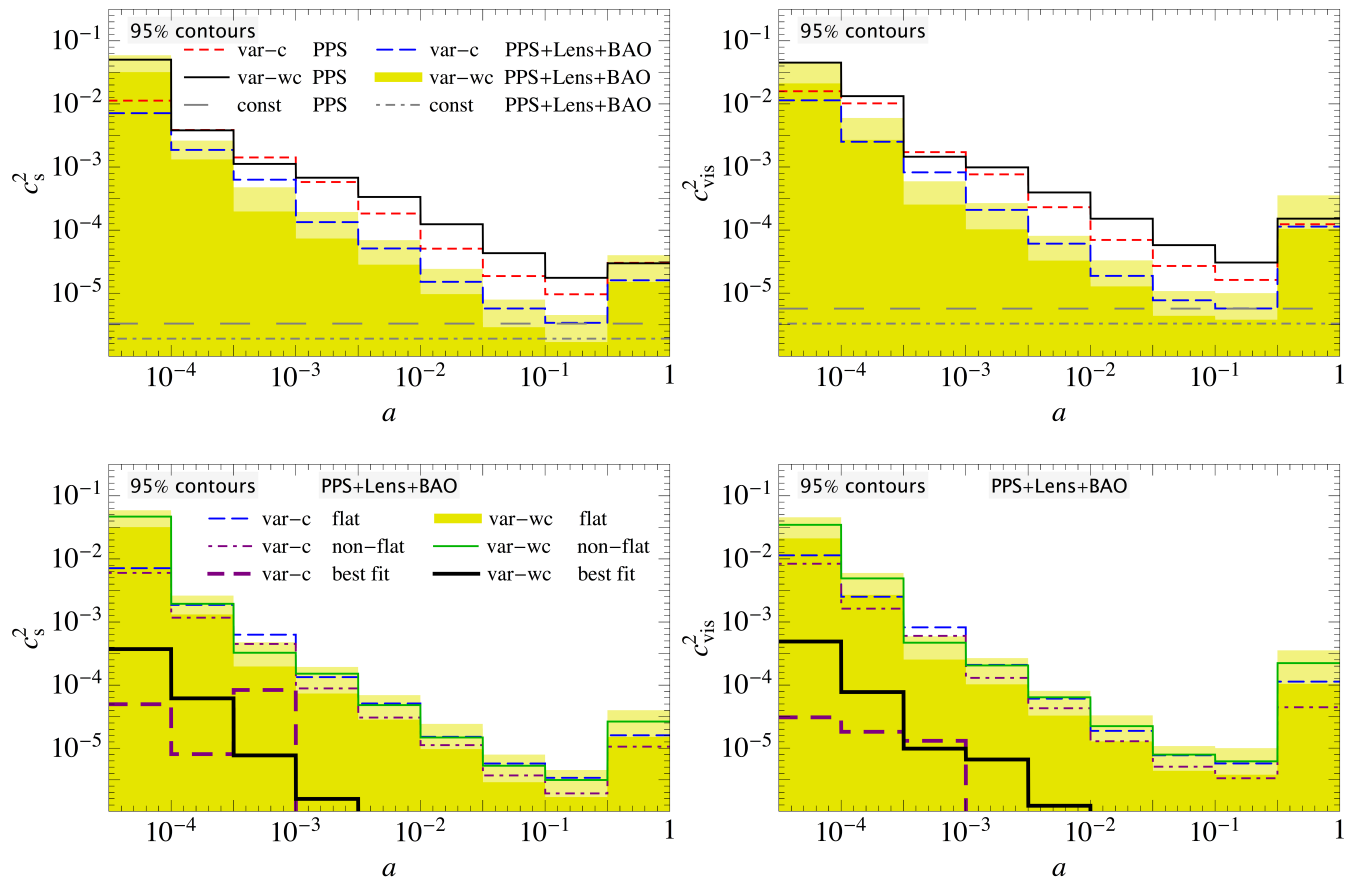


FIG. 4. The upper panels display the 95% credible regions of c_s^2 (left) and c_{vis}^2 (right) when PPS alone and the PPS+Lens+BAO dataset combination was used for constraining the *var-c* and *var-wc* models. The constraints on constant c_s^2 and c_{vis}^2 parameters from [44] are superimposed in grey. The lower panels display the 95% credible regions of c_s^2 (left) and c_{vis}^2 (right) when the PPS+Lens+BAO dataset combination was used, showing the effect of having nonflat priors as well as the best fit model. In all panels does the darker yellow shading display the 68% confidence regions. Note that the vertical axis is logarithmic so that the constraining power of the later universe data is quite drastic compared to the early universe data.

Fig. 4.⁵

2. Constraints on the $c_{+,i}^2$ and b combinations

In Table V (see Appendix C) we summarize the constraints on $c_{+,i}^2$ in the nonflat prior case. The shape of the upper limits on $c_{+,i}^2$ follows those of $c_{s,i}^2$ (and of $c_{\text{vis},i}^2$) shown in the lower panels of Fig. 4, but are about a factor of 3 larger. This is partly a consequence of error propagation and partly an effect of the nonflat priors. We remind the reader that “nonflat” priors refer to *flat priors* on $c_{+,i}^2$ and b_i as described in detail in Sec. III C and specifically (3.2). Thus constraints on $c_{s,i}^2$ and c_{vis}^2 are stronger than those on $c_{+,i}^2$.

Interpreting the constraints on $c_{+,i}^2$ by imposing flat priors on $c_{s,i}^2$ and $c_{\text{vis},i}^2$ is difficult since even a uniform 2D-posterior in the $c_{s,i}^2$ - $c_{\text{vis},i}^2$ quadrant would lead to a peak at nonzero $c_{+,i}^2$ for the 1D-posterior of $c_{+,i}^2$. This may be understood through (3.3) which implies that the 1D-marginalized prior for $c_{+,i}^2$ is proportional to $c_{+,i}^2$. The parameter $0 < b < 1$ remains largely unconstrained at present. It is expected, however, that structure formation data which include smaller scales could provide constraints on b , or put differently, break the degeneracy between c_s^2 and c_{vis}^2 [43].

C. Degeneracies and shifts in the credible regions

In Fig. 5 we display several 2D-posteriors for the models considered when the PPS+Lens+BAO dataset combination was used. As evidenced by this figure the best-fit parameters of the models containing $c_{s,i}^2$ and $c_{\text{vis},i}^2$ (that is *var-wc* and *var-c*) lie significantly outside their credible regions. This is

⁵ Note that there are only upper limits on the perturbative GDM parameters and their best fit value are always significantly closer to zero than their upper limit.

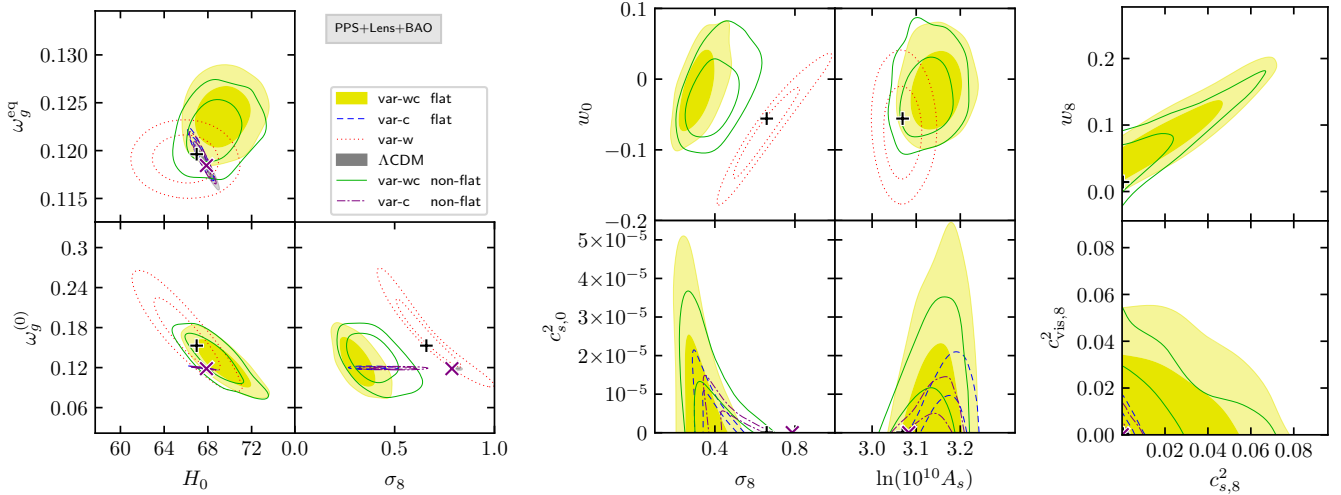


FIG. 5. The 2D contours of the 68% and 95% credible regions of various parameter combinations in the set $\{\omega_g^{(0)}, \omega_g^{\text{eq}}, H_0, \sigma_8, w_0, w_8, A_s, c_{s,0}^2, c_{s,8}^2, c_{\text{vis},8}^2\}$ when the PPS+Lens+BAO dataset combination was used, showing the effect of nonflat priors. Displayed are the *var-wc* model with flat priors (yellow shades) and nonflat priors (green lines), the *var-c* model with flat priors (blue dashed lines) and nonflat priors (purple dot-dashed lines), the *var-w* model (red dotted lines) and Λ CDM (grey shades). The best-fit points are indicated by a black plus for the *var-wc* and purple cross for the *var-c* model.

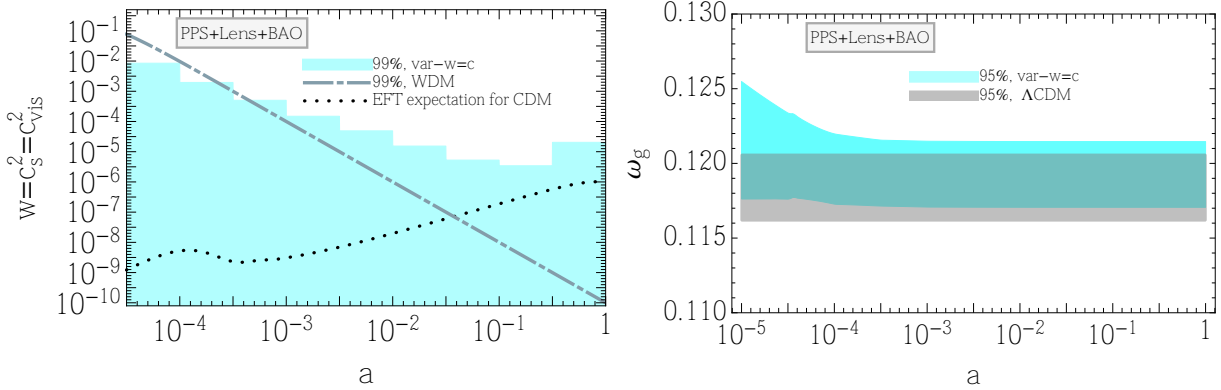


FIG. 6. *Left*: Shown are the 99% credible regions (shaded blue) of $w_i = c_{s,i}^2 = c_{\text{vis},i}^2$ model when the dataset combination PPS+Lens+BAO was used. The blue dot-dashed line is the constraint from [32] while the dotted line is the rough expectation from the EFTofLSS [see 28]. *Right*: 95% credible regions on $\omega_g(a)$ contrasted with those of Λ CDM in grey.

a consequence of the location of the peak of our likelihood (i.e. the best-fit point) being close to the border of our prior volume, which itself has a nontrivial shape. The best-fit point of the *var-wc* model is marked with a black plus sign and the corresponding one for the *var-c* submodel with a purple cross. Choosing nonflat priors reduces, quite generally, the distance between the best-fit points and the credibility contours, confirming our suspicion that the effects coming from a choice of priors may be responsible. We find that the best-fit parameters lie within the credible regions of the corresponding nested models with $c_{s,i}^2 = c_{\text{vis},i}^2 = 0$, consistent with the fact that adding the perturbative GDM parameters does not increase the goodness of fit. Specifically, the best-fit point of *var-wc* lies inside the 68% credible region of *var-w*, and similarly the best-fit point of *var-c* lies inside the 68% credible region of

Λ CDM.

As was already observed when constraints on constant GDM parameters were obtained in an earlier work [44], there is a degeneracy between the present day values $\omega_g^{(0)}$, H_0 and w_0 . This degeneracy persists also in the *var-wc* model.

Even more interesting are the various shifts of the credible region contours of the *var-wc* model (yellow shades and green lines) with respect to either the *var-w* (red dotted) or the Λ CDM models. For some parameter combinations, a shift is also seen between the *var-c* (blue dashed and purple dot-dashed) and the *var-w*/ Λ CDM models, e.g. in the $\{\omega_g^{(0)}, \sigma_8\}$ -plane, while for others no such shift is observed. Thus these shifts occur through the interplay between w and c_s^2 and c_{vis}^2 .

The most important shift is the one occurring in the ω_g^{eq} -

H_0 and $\omega_g^{(0)}$ - H_0 planes, both cases involving H_0 . This shift allows the Hubble constant H_0 to be pushed to higher values today $H_0 = 69.3^{+3.3}_{-3.0}$ than the Λ CDM value $H_0 = 67.89^{+0.93}_{-0.93}$, while keeping $\omega_g^{(0)}$ centered closer to the Λ CDM value than in the case of the *var-w* model. The physical mechanism for the increased value of H_0 is related to the increased value of ω_g^{eq} and is discussed below in Sec. V.

Another shift occurs in the clustering strength at late times, σ_8 , and at early times, A_s seen in the middle panel of Fig. 5. While the presence of non-negative c_s^2 and c_{vis}^2 in the *var-c* model is sufficient to shift σ_8 toward smaller values compared to Λ CDM, in combination with letting w free in the *var-wc* model, the σ_8 parameter shifts to even smaller values, while A_s increases, see the middle panel of Fig. 5. The increase in A_s is a consequence of the w_8 - $c_{s,8}^2$ degeneracy seen in the right panel of Fig. 5. As we explain in Sec. V the w_8 - $c_{s,8}^2$ degeneracy is caused by properties of the adiabatic initial conditions in the GDM model. This degeneracy, in combination with the positivity of $c_{s,8}^2$, is also responsible for the increase in ω_g^{eq} and all the other shifts discussed above.

It is also worth pointing out that the usual degeneracy between c_s^2 and c_{vis}^2 which keeps the combination $c_+^2 = c_s^2 + \frac{8}{15}c_{\text{vis}}^2$ constant is broken in bin 8 for the case of the *var-wc* model, as seen on the lower right panel of Fig. 5. This is because of the dependence of the adiabatic initial conditions on w_8 , $c_{s,8}^2$ and $c_{\text{vis},8}^2$. The adiabatic initial conditions may be found in [28], however, (5.1) below shows how this effect works. This degeneracy is restored in the later bins, which is reflected in the red, and thus positive, diagonal in the $c_{s,i}^2$ - $c_{\text{vis},i}^2$ correlation matrix displayed in Fig. 10 (see Appendix C).

D. Constraints on the submodel *var-w=c*

The final submodel of *var-wc* we study is the case where $w_i = c_{s,i}^2 = c_{\text{vis},i}^2$, denoted by *var-w=c*. This case is interesting because freely streaming matter satisfies this condition either exactly (in case of ultrarelativistic radiation), or approximately. One example of the latter is the warm dark matter (WDM) model. A second example of an approximate $w_i = c_{s,i}^2 = c_{\text{vis},i}^2$ relation is the CDM model on linear scales with the inclusion of backreaction terms coming from integrating out nonlinear scales as in the effective field theory of large-scale structure [EFTofLSS, 9, 15, 16, 19].

In the left panel of Fig. 6 we show our constraints on the $w_i = c_{s,i}^2 = c_{\text{vis},i}^2$ submodel in shaded blue. We superimpose the WDM constraints from [32] (dot-dashed line) where approximately $w = c_s^2 = c_{\text{vis}}^2 = (\frac{1}{3} + \frac{c_{s,0}^2}{a^2})^{-1}$ and also a rough estimate for the EFTofLSS (black dashed line) discussed in [28].

In the right panel we show the derived parameter $\omega_g(a)$. Comparing to *var-wc* and other submodels in Fig. 3, it is clear that the DM abundance in this submodel is much more tightly constrained. This is due to the much tighter constraints on w_i which in the late universe are driven by the upper limits on $c_{s,i}^2 = c_{\text{vis},i}^2$ which cannot be larger than the upper limits on $\{w_i, c_{s,i}^2, c_{\text{vis},i}^2\}$ in the *var-wc* model, so that they approximately

follow those of $c_{+,i}^2$ in Table V. The constraints on standard cosmological parameters in the *var-w=c* model are as tight as in Λ CDM, with all 2D-posteriors overlapping except for σ_8 caused by the diminished DM growth due to the non-negative sound speed and viscosity. The constraint on the Hubble constant $H_0 = 67.60^{+0.96}_{-0.93}$ (95%.C.L.) is virtually the same as corresponding Λ CDM value of $H_0 = 67.89^{+0.93}_{-0.93}$.

A recurring theme throughout our results is the improvement of the constraints on c_s^2 and c_{vis}^2 due to the CMB lensing spectrum, which is most significant for bin 1 (as shown by Fig. 4). The lensing spectrum used in this work will be substantially improved by upcoming CMB experiments, such as Simons Observatory [1, see Fig. 6 in that work for the expected improvement in the noise compared to the data used in this paper]. This improvement from upcoming surveys is particularly significant given the EFTofLSS model line in Fig. 6. This model has no free amplitude parameter that can be used to shift the model prediction up or down, and the upper limit we have achieved in bin 1 is only a factor of a few above the model. Given that this bin benefits the most by the inclusion of the lensing spectrum, a detection of an EFTofLSS-type GDM signal is likely with the improved lensing spectrum from upcoming experiments.

V. DISCUSSION AND IMPLICATIONS

In this section we discuss the physical mechanism underlying our most interesting results, namely the increase of ω_g in the early universe, leading to an increase of H_0 for the *var-wc* model.

Let us first examine the origin of the increase of ω_g^{eq} , the value of ω_g at matter-radiation equality, in the *var-wc* model compared to either *var-w* or Λ CDM. Increasing ω_g^{eq} is ultimately tied to *var-wc* favoring a higher EoS w in the early universe. To exemplify, the heights of the CMB peaks severely constrain the evolution of the potential Φ between radiation and matter eras. Specifically, Φ can only evolve within a narrow band of allowed values, otherwise it would cause either too much or too little early ISW and acoustic driving in the CMB. These two effects are controlled by a_{eq} which in turn translates to a small range of allowed values for w_{eq} (leading to the w_{eq} - ω_g^{eq} degeneracy).

Now, during the matter era Φ is closely linked to the GDM comoving density perturbation $\Delta_g = \delta_g + 3aH(1+w)\theta_g$, hence, this narrow band of values for Φ translates to an equivalent range in Δ_g . However, during the radiation era Φ is sourced by $\Delta_{\text{radiation}}$ and thus the link to Δ_g is broken. Therefore, the data select trajectories for Δ_g which may start within a fairly wide range of initial values but subsequently all squeeze within a narrow range of values around the time of matter-radiation equality. This is precisely what is observed in Fig. 7. There we plot the evolution of a single k -mode ($k = 0.085\text{Mpc}^{-1}$) of Δ_g for a representative sample of our Monte Carlo Markov Chains color-coded by their w_8 value. The effect just described is clearly visible in all panels, but less so in the left which displays the Δ_g evolution in the *var-w* submodel. This behavior is similar to the GDM abundance ω_g which squeezes

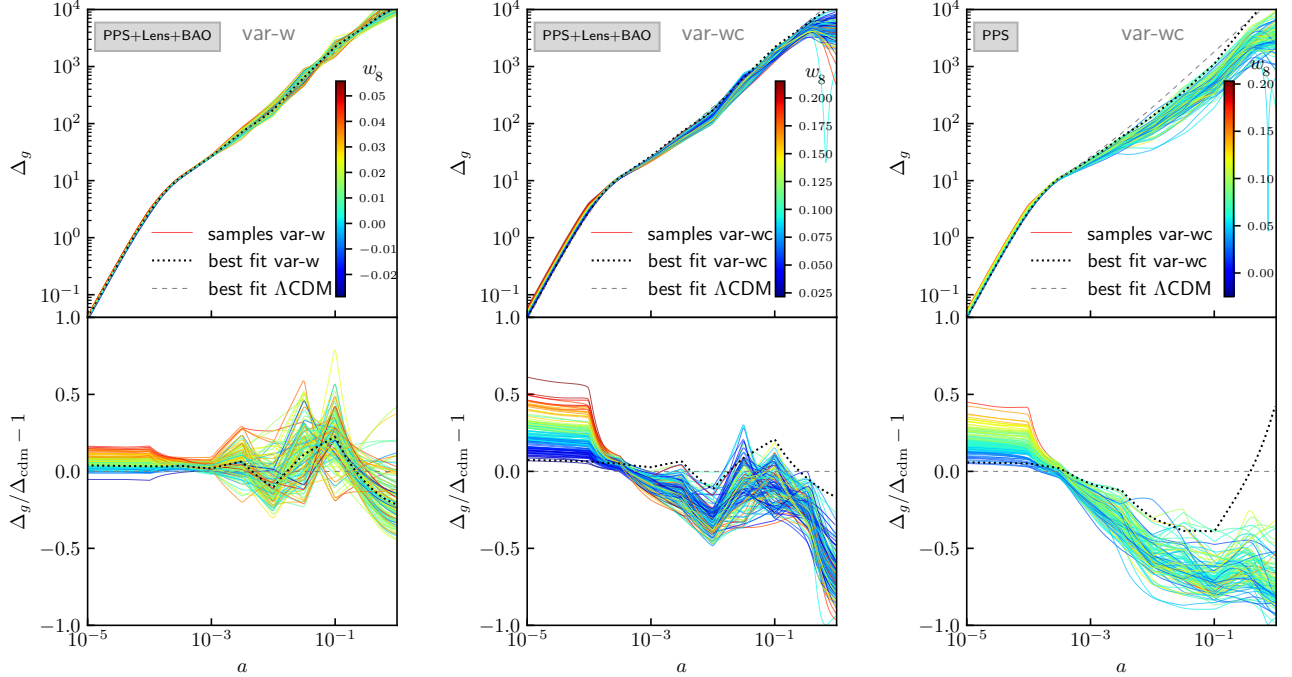


FIG. 7. Samples from a MCMC chain, showing the evolution of the GDM comoving density perturbation $\Delta_g(a)$ at a fixed scale $k = 0.085 \text{ Mpc}^{-1}$. In the lower set of panels we show the relative difference compared to the ΛCDM best-fit in order to make the effects described in the text more visible. Just as in the case of $\omega_g(a)$, $\Delta_g(a)$ also squeezes to a small allowed range around the time of matter-radiation equality a_{eq} . This is facilitated by a spread at early times due to the w -dependence of the time evolution of superhorizon modes during the radiation era. On the *left* we show the case of the *var-w* model which is to be contrasted with the *var-wc* model in the *middle* panel, both according to the PPS+Lens+BAO dataset combination. The degeneracy between $c_{s,8}^2$ and w_8 in the adiabatic mode solution during that time shifts the distribution to larger and positive values of w_8 as compared to *var-w*. The *right* panel shows the evolution of $\Delta_g(a)$ in *var-wc* model according to PPS alone. Observe that the best fit (dotted) is not affected by this shift but it remains close to the ΛCDM case (dashed).

within a narrow range of values around a_{eq} in Fig. 3. Thus, the CMB constrains both the DM abundance and the amplitude of DM perturbations most strongly around a_{eq} .

Although the squeeze in Δ_g is present in both models, in the *var-wc* model it is more pronounced. The reason is that the evolution of Δ_g is affected by both w and c_s^2 . Meanwhile, during the radiation dominated era, the GDM density perturbation in the synchronous gauge evolves on large scales ($k\eta \ll 1$) as

$$\delta_g = \zeta_{\text{ini}} \left(-\frac{1}{4} + \frac{3c_s^2 - 5w}{8} \right) (k\eta)^2, \quad (5.1)$$

when adiabatic initial conditions specified by the initial curvature perturbation ζ_{ini} are set [28]. Therefore, the GDM parameters w_8 and $c_{s,8}^2$ affect the initial amplitude of the GDM density perturbations and consequently the initial Δ_g . While w_8 takes both positive and negative values, $c_{s,8}^2$ must be non-negative. The two compensate each other only for $w_8 > 0$, implied by (5.1), leading to the degeneracy shown in the right panel of Fig. 5. However, the slope of the degeneracy is not what one would expect from (5.1) under the naive assumption $\Delta_g^{\text{ini}} = \Delta_{\text{cdm}}^{\text{ini}}$, because both w_8 and $c_{s,8}^2$ affect the subsequent evolution of Δ_g into the squeezed region around a_{eq} . Nevertheless, this degeneracy combined with the squeezed region around a_{eq} drive the posteriors of both w_8 and $c_{s,8}^2$ to more

positive values. Due to the $w - \omega_g$ degeneracy discussed first in [23] and recently demonstrated in [44], once w_8 shifts to positive values it then leads to an increase of the early universe abundance of DM $\omega_g^{(8)}$ and consequently ω_g^{eq} .

Before discussing the increase of H_0 in the *var-wc* model, we briefly comment on a few minor points. First, we showed in Sec. IV that marginalizing over c_s^2 and c_{vis}^2 in the *var-wc* model does not exactly lead to the same posteriors as in the *var-w* submodel where $c_s^2 = c_{\text{vis}}^2 = 0$. This is a consequence of our discussion of the w_8 and $c_{s,8}^2$ degeneracy combined with the squeeze in Δ_g at equality. Second, adding the Lens dataset widens the 1D-posteriors of $c_{s,8}^2$, compared to PPS alone, a somewhat counter-intuitive result also inferred from Table III. In the right of Fig. 7 we plot the Δ_g samples using PPS alone, showing a distribution of curves shifted toward smaller $\Delta_g/\Delta_{\text{cdm}} - 1$ in the late universe. This is the result of diminished constraining power on DM clustering at that time and since growth is an integrated effect, the drop of $\Delta_g/\Delta_{\text{cdm}} - 1$ then requires a more CDM-like growth in the early universe, thus favoring smaller values of $c_{s,8}^2$. Lastly, since $c_{s,8}^2$ and w_8 are correlated, adding the Lens dataset favors larger values of w_8 and explains why this dataset affects significantly the constraints on w_8 in the *var-wc* model.

We now discuss the reasons for the increase of the mean of H_0 in the *var-wc* model, making H_0 more consistent with su-

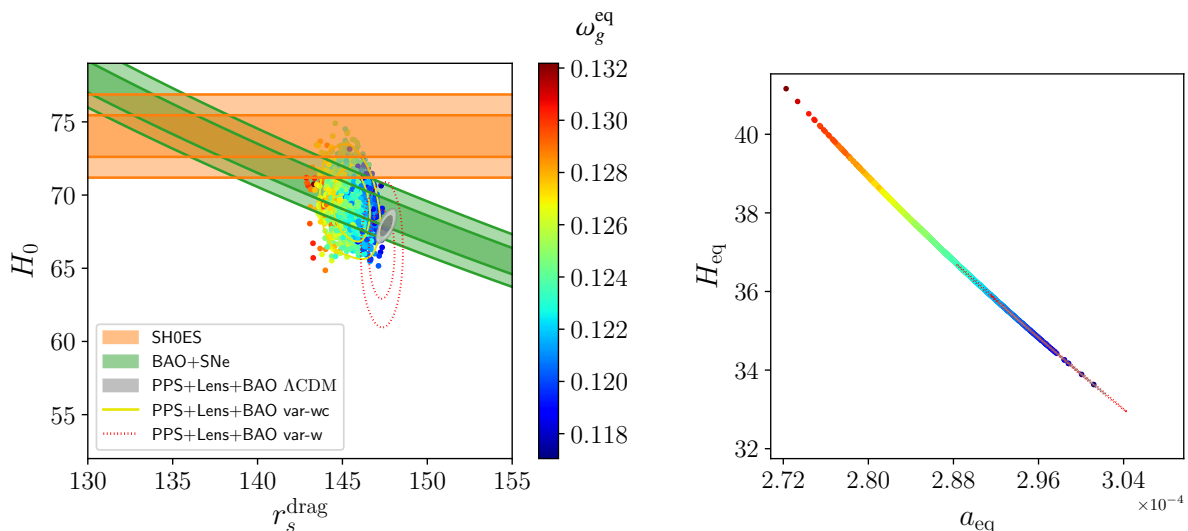


FIG. 8. *Left*: We show the 68% and 95% credible regions for various datasets and models used to constrain H_0 and r_s^{drag} . The SH0ES and the BAO+SNe credible regions are adopted from [27]. *Right*: We show the 68% and 95% credible regions of the H_{eq} and a_{eq} plane, demonstrating that ω_g^{eq} uniquely determines H_{eq} and a_{eq} .

pernovae estimates of its value. As was explained in [29], there is strong degeneracy between $\omega_g^{(0)}$, w_0 and H_0 in the *var-w* model, since these late universe parameters determine a large fraction of the angular diameter distance d_A^* to the last scattering surface. This degeneracy is still observed to be present in the *var-wc* model. However, as can be seen in the left panel of Fig. 5, the contours in the $\omega_g^{(0)} - H_0$ plane shift to larger values of H_0 and smaller values of $\omega_g^{(0)}$ along the degeneracy direction, compared to the *var-w* case. This happens because increasing w_0 allows easier structure growth in the late universe (see $w_0 - \sigma_8$ degeneracy in Fig. 5 and App. A). In the *var-wc* model the perturbative GDM parameters shift σ_8 to small values and the more negative values of w_0 become disfavored by CMB lensing, so that overall w_0 tends to be more positive. This tighter and more positive distribution of w_0 then leads to a tighter distribution of $\omega_g^{(0)}$ with smaller mean (compared to *var-w*). Therefore a larger H_0 compared to *var-w* is required to get the right d_A^* .

However, the mean of $\omega_g^{(0)}$ in the *var-wc* model is not too different from its values in Λ CDM and hence, there is more to this story. The intrinsic size of the sound horizon at the end of recombination, or rather the baryon drag epoch, r_s^{drag} , is different in *var-wc* case. As was pointed out in [27], an increase in r_s^{drag} is one of the most natural ways for increasing H_0 as inferred from early universe data and in turn relaxing the H_0 -tension.

In Fig. 8 we reproduce Fig.1 of [27], showing two model independent constraints in the $H_0 - r_s^{\text{drag}}$ plane from distance ladder-calibrated supernovae (SH0ES) and supernovae-calibrated angular diameter distance measurements of r_s^{drag} (BAO+SNe). We replaced the high- ℓ and low- ℓ Λ CDM constraints which were part of the original figure by several GDM constraints on H_0 and r_s^{drag} coming from the PPS+Lens+BAO

dataset combination. We show the 68% and 95% credible regions for the *var-wc* model (yellow curves), Λ CDM (grey) and *var-w* (red dotted), and additionally a set of samples color-coded according to ω_g^{eq} using the *var-wc* model. While the original Fig.1 of [27] revealed that changing $\omega_g^{(0)}$ cannot reconcile SH0ES and BAO+SNe, it is clear from our Fig. 8 that an independent increase of ω_g^{eq} can move the contours to larger r_s^{drag} and larger H_0 toward a region where SH0ES and BAO+SNe overlap.

As is clear from the right panel of Fig. 8, ω_g^{eq} is uniquely tied to H_{eq} and a_{eq} , such that r_s^{drag} is larger due to an increase in the prerecombination Hubble parameter and earlier matter-radiation equality (while keeping $\omega_g^{(0)}$ at a smaller value). Thus, an increased ω_g^{eq} , whose origin we already explained above, is the source of an increased H_0 in the *var-wc* model.

We note in passing that although the *var-w=c* submodel allows in principle for $\omega_g^{\text{eq}} > \omega_g^{(0)}$, the data does not favor such a shift. We see in Fig. 6 that ω_g^{eq} is very close to $\omega_g^{(0)}$, which in turn is very close to the Λ CDM value. This results in a low H_0 value which is comparable to that of Λ CDM, so that a *var-w=c* type model cannot resolve the H_0 tension.

Our analysis indicates that a designed GDM model with only a couple of additional parameters from Λ CDM (rather than 26) may be able to address and further investigate the H_0 and σ_8 tensions. Our models also further elucidate the mechanism by which decaying dark matter, see e.g. [12, 13, 47] can increase the CMB inference of H_0 and decrease σ_8 . Such a model naturally implements a positive w_8 and $c_{s,8}^2$ when decaying DM and dark radiation are collectively modeled as a single GDM fluid.

Finally, we note that in our analysis we assumed that dark energy is a cosmological constant. Letting the dark energy EoS vary in redshift could, in principle, lead to degeneracies

with w (dark matter EoS). The case of late DE was investigated in [46], where the degeneracy was solved by using both early- and late-time observables of the perturbations – for instance, CMB data combined with a forecast for galaxy clustering data. It is also possible to have an early dark energy (EDE) component (see e.g. [22, 26]). If the EDE is uncoupled with the DM and has negligible perturbations, or if the EDE is tightly-coupled with the DM, the combined EDE+DM fluid can be well described by a single GDM fluid [28], so that one could interpret our constraints on GDM parameters as constraints on such mixture scenarios. An EDE component which is not tightly-coupled to the DM is unlikely to be the cause of the early-time marginal effects discussed in this section, since for those effects to appear a varying DM sound speed is necessary, and in addition, they do not occur when only the EoS is varied.

VI. CONCLUSION

We have presented the most exhaustive parameter search of DM properties to date, using the generalized dark matter model (GDM). We allowed all three GDM parametric functions to have a fairly general time dependence by binning w in 8 and c_s^2 and c_{vis}^2 in 9 scale factor bins, that is, 26 new parameters beyond Λ CDM in total. We found no convincing evidence for any of these parameters to be nonzero. We expect that merging some bins will tighten the constraints for each bin; however, we do not expect that significant non-CDM behavior would emerge as even in the extreme case of constant GDM parameters, this doesn't happen. Thus, our result should be seen as depicting the most general time-variation of DM properties allowed by the data.

We analyzed four nested models: *var-wc* (all 26 parameters free), *var-c* (setting $w_i = 0$), *var-w* (setting $c_s^2 = c_{\text{vis}}^2 = 0$; previously studied in [29]) and *var-w=c* where the constraint $w = c_s^2 = c_{\text{vis}}^2$ was imposed. Our strongest constraints on w were in the early universe around matter-radiation equality, while the strongest constraints on c_s^2 and c_{vis}^2 are between redshift 2 and 9 where the constraining power of the CMB lensing peaks.

Our analysis was performed using flat and nonflat priors for the perturbative GDM parameters, in order to ensure robustness of the results. Indeed, while three early universe bins show significant shifts for w away from zero in the *var-wc* model when flat priors were used, these become less significant when nonflat priors were used.

Having a varying w improved the fits marginally while letting c_s^2 and c_{vis}^2 be free led to virtually no improvement. However, c_s^2 and c_{vis}^2 introduced some rather interesting features. We observed a number of interesting shifts in the 2D posteriors between the *var-w* and *var-wc* models. Specifically, the *var-wc* model shifts the DM abundance around equality ω_g^{eq} to higher values while today $\omega_g^{(0)}$ decreases and the Hubble constant H_0 increases compared to *var-w* or to Λ CDM. Interestingly, σ_8 also shifts to lower values in the *var-wc* model. These shifts indicate the potential of GDM to alleviate the H_0 and σ_8 tensions driven by early and late universe data. In particular, an *a-posteriori* constructed GDM model with only a couple of more parameters than Λ CDM may be favored over the latter while simultaneously addressing these tensions. Our present analysis paves the way for further work in this direction using more recent cosmological datasets [e.g 40] as well as investigating possible k^2 -dependencies in the c_s^2 and c_{vis}^2 parametric functions.

Finally, we reiterate our assertion that upcoming CMB experiments, such as Simons Observatory [1] will substantially improve the CMB lensing constraining power. This improvement is expected to have profound impact on further constraining and quite possibly detecting DM properties in the late universe, specifically c_s^2 and c_{vis}^2 . We predict that a detection of an EFTofLSS type GDM signal is likely with the improved lensing spectrum from upcoming experiments.

ACKNOWLEDGMENTS

The research leading to these results has received funding from the European Research Council under the European Union's Seventh Framework Programme (FP7/2007-2013) / ERC Grant Agreement no. 617656 "Theories and Models of the Dark Sector: Dark Matter, Dark Energy and Gravity". The Primary Investigator is C. Skordis.

-
- [1] Ade, P. et al. 2019, JCAP, 1902, 056
 - [2] Aguilar, M., Ali Cavasonza, L., Ambrosi, G., et al. 2019, Phys. Rev. Lett., 122, 041102
 - [3] Ahlers, M., Mertsch, P., & Sarkar, S. 2009, Phys. Rev., D80, 123017
 - [4] Anderson, L., Aubourg, É., Bailey, S., et al. 2014, MNRAS, 441, 24
 - [5] Aprile, E. et al. 2018, Phys. Rev. Lett., 121, 111302
 - [6] Aprile, E. et al. 2019, Phys. Rev. Lett., 122, 141301
 - [7] Aprile, E. et al. 2019, Phys. Rev. Lett., 123, 251801
 - [8] Aprile, E. et al. 2019, Phys. Rev. Lett., 123, 241803
 - [9] Baumann, D., Nicolis, A., Senatore, L., & Zaldarriaga, M. 2012, JCAP, 7, 51
 - [10] Bertone, G., Hooper, D., & Silk, J. 2005, Phys. Rept., 405, 279
 - [11] Beutler, F., Blake, C., Colless, M., et al. 2011, MNRAS, 416, 3017
 - [12] Bringmann, T., Kahlhoefer, F., Schmidt-Hoberg, K., & Walia, P. 2018, Phys. Rev. D, 98, 023543
 - [13] Buen-Abad, M. A., Schmaltz, M., Lesgourgues, J., & Brinckmann, T. 2018, JCAP, 2018, 008
 - [14] Calabrese, E., Migliaccio, M., Pagano, L., et al. 2009, Phys. Rev. D, 80, 063539
 - [15] Carrasco, J. J. M., Hertzberg, M. P., & Senatore, L. 2012, JHEP, 09, 082
 - [16] Carroll, S. M., Leichenauer, S., & Pollack, J. 2014, Phys. Rev., D90, 023518

- [17] Feroz, F., Hobson, M. P., & Bridges, M. 2009, MNRAS, 398, 1601
- [18] Ferreira, P. G. & Skordis, C. 2010, Phys. Rev., D81, 104020
- [19] Foreman, S. & Senatore, L. 2016, JCAP, 1604, 033
- [20] Foreman-Mackey, D., Hogg, D. W., Lang, D., & Goodman, J. 2013, PASP, 125, 306
- [21] Goodman, J. & Weare, J. 2010, Communications in Applied Mathematics and Computational Science, 5, 65
- [22] Hill, J. C., McDonough, E., Toomey, M. W., & Alexander, S. 2020, Phys. Rev. D, 102, 043507
- [23] Hu, W. 1998, Astrophys.J., 506, 485
- [24] Ilić, S. 2021, in preparation
- [25] Kaplinghat, M., Knox, L., & Skordis, C. 2002, ApJ, 578, 665
- [26] Karwal, T. & Kamionkowski, M. 2016, Phys. Rev. D, 94, 103523
- [27] Knox, L. & Millea, M. 2020, Phys. Rev. D, 101, 043533
- [28] Kopp, M., Skordis, C., & Thomas, D. B. 2016, Phys. Rev. D, 94, 043512
- [29] Kopp, M., Skordis, C., Thomas, D. B., & Ilić, S. 2018, Phys. Rev. Lett., 120, 221102
- [30] Kumar, S., Nunes, R. C., & Yadav, S. K. 2019, MNRAS, 490, 1406
- [31] Kumar, S. & Xu, L. 2014, Physics Letters B, 737, 244
- [32] Kunz, M., Nesseris, S., & Sawicki, I. 2016, Phys. Rev. D, 94, 023510
- [33] Lesgourgues, J. 2011, arXiv e-prints, arXiv:1104.2932
- [34] Lesgourgues, J. & Tram, T. 2011, JCAP, 9, 32
- [35] Lewis, A. 2019, arXiv e-prints, arXiv:1910.13970
- [36] Manzotti, A. 2018, Phys. Rev., D97, 043527
- [37] Mertsch, P. & Sarkar, S. 2014, Phys. Rev., D90, 061301
- [38] Müller, C. M. 2005, Phys. Rev. D, 71, 047302
- [39] Planck Collaboration, Ade, P. A. R., Aghanim, N., et al. 2016, A&A, 594, A13
- [40] Planck Collaboration, Aghanim, N., Akrami, Y., et al. 2020, A&A, 641, A6
- [41] Planck Collaboration, Aghanim, N., Arnaud, M., et al. 2016, A&A, 594, A11
- [42] Riess, A. G., Macri, L., Casertano, S., et al. 2011, ApJ, 730, 119
- [43] Thomas, D. B., Kopp, M., & Markovič, K. 2019, MNRAS, 490, 813
- [44] Thomas, D. B., Kopp, M., & Skordis, C. 2016, ApJ, 830, 155
- [45] Tutusaus, I., Lamine, B., & Blanchard, A. 2018, arXiv e-prints, arXiv:1805.06202
- [46] Tutusaus, I., Lamine, B., Blanchard, A., et al. 2016, Phys. Rev., D94, 123515
- [47] Vattis, K., Koushiappas, S. M., & Loeb, A. 2019, Phys. Rev. D, 99, 121302
- [48] Wang, L. & Steinhardt, P. J. 1998, ApJ, 508, 483
- [49] Xu, L. & Chang, Y. 2013, Phys. Rev. D, 88, 127301

Appendix A: The DM growth rate in a Λw DM universe

1. Derivation of the growth rate formula

Here we derive the DM growth rate in the GDM model with constant w equation of state and zero perturbative parameters, i.e. $c_s^2 = c_{\text{vis}}^2 = 0$, assuming that the only components affecting the late Universe is GDM and cosmological constant Λ .

Hence, we have

$$\Omega_g + \Omega_\Lambda = 1 \quad (\text{A1})$$

$$\Omega_g = \frac{\Omega_{0g}}{\Omega_{0g} + (1 - \Omega_{0g})a^{3(1+w)}} \quad (\text{A2})$$

where Ω_{0g} is the relative GDM density today.

Consider now the gauge-invariant Bardeen potentials

$$\Phi = -\frac{h + k^2 v}{6} + \frac{1}{2} a^2 H \dot{v} \quad (\text{A3})$$

$$\Psi = -\frac{1}{2} a^2 \ddot{v} - a^2 H \dot{v} \quad (\text{A4})$$

corresponding to the conformal Newtonian gauge metric perturbations. Exchanging Ψ with the gauge-invariant metric variable

$$\mathcal{R} = \Phi + \frac{2}{3} \frac{\dot{\Phi} + H\Psi}{(1+w)H} \quad (\text{A5})$$

we find that the evolution of Φ and \mathcal{R} is dictated by

$$H^{-1} \dot{\Phi} = \frac{3}{2} (1+w) \Omega_g (\mathcal{R} - \Phi) - \Phi \quad (\text{A6})$$

$$H^{-1} \dot{\mathcal{R}} = 0, \quad (\text{A7})$$

which is a special case of the more general case where c_s^2 and c_{vis}^2 are nonzero, as presented in [28]. The solution is given in terms of the ordinary hypergeometric function ${}_2F_1$ as

$$\Phi = \Phi_{\text{ini}} \left[\frac{5+3w}{3(1+w)} - \frac{{}_2F_1\left(\frac{1}{2}, \frac{5+3w}{6(1+w)}, \frac{11+9w}{6(1+w)}, -\frac{\Omega_\Lambda}{\Omega_g}\right)}{\sqrt{\Omega_g}(5+3w)} \right] \quad (\text{A8})$$

$$\mathcal{R} = \frac{5+3w}{3(1+w)} \Phi_{\text{ini}} = \text{const.} \quad (\text{A9})$$

where Φ_{ini} is an initial condition.

The above exact solution is not particularly useful. A more useful result is obtained by observing that the growth of Φ is scale independent and thus we can define $\gamma(a)$ via $d\Phi/d \ln a = \Phi(\Omega_g^\gamma - 1)$ and use Ω_g as the time variable [see e.g. 18]. Using $d\Omega_g/d \ln a = 3(1+w)(1-\Omega_g)\Omega_g$ we find that the evolution equation (A6) for Φ simplifies to

$$\Phi \Omega_g^\gamma = \frac{3}{2} (1+w) \Omega_g (\mathcal{R} - \Phi) \quad (\text{A10})$$

$$\Rightarrow \Phi = \frac{5+3w}{2\Omega_g^{\gamma-1} + 3(1+w)} \Phi_{\text{ini}}, \quad (\text{A11})$$

where (A9) was used and where $\gamma(\Omega_g)$ is at this point still undetermined.

We proceed to find an approximate solution for $\gamma(\Omega_g)$ assuming that Ω_Λ is small and Taylor expand the equation for γ (by plugging (A11) back into (A6)) around $\Omega_\Lambda = 0$ (thus around w DM dominated era). This leads to a hierarchy of algebraic equations for the Taylor coefficients of γ . The lowest two give

$$\gamma = \frac{6(1+w)}{11+9w} \left[1 + \frac{\Omega_\Lambda(1+3w)(5+3w)}{2(11+9w)(17+15w)} + \mathcal{O}(\Omega_\Lambda^2) \right]. \quad (\text{A12})$$

This approximation is accurate to 1% for $\Omega_g^{(0)} > 0.2$ and $a \leq 1$. The expression reduces to the standard Λ CDM result when $w = 0$ [18]. Beware also that w here is for DM, not dark energy. Hence, the formula for γ above, differs from the usual Wang-Steinhardt result [18, 48].

2. Integrated Sachs-Wolfe effect

Define the growth factor

$$D(a) \equiv \Phi / \Phi_{\text{ini}}. \quad (\text{A13})$$

Then in the case $\Omega_\Lambda = 0$ we obtain $D = 1$ and thus as explained in [28] there is no integrated Sachs-Wolfe (ISW) effect in a w DM dominated universe. However, in a Λw DM universe w can directly affect the late ISW effect.

Evaluating $D(a)$ at $a = 1$ we find that for sensible values of w and fixed $\Omega_g^{(0)}$ the change to the Λ CDM late ISW effect are small. A positive (negative) w gives rise to less (more) potential decay, as might be anticipated from the fact that the absolute value of $w_{\text{tot}} = \Omega_g(1+w) - 1$ is reduced (increased). For the case $\Omega_g^{(0)} = 0.3$ we find a 2% deviation of D between the cases $w_0 = 0.1$ and $w_0 = 0$ and thus given any fixed $\Omega_g^{(0)}$ the effect of nonzero w on the ISW is negligible. Any role played by w to affect the late ISW effect in GDM is thus dominated by a free w to increase the allowed range for $\Omega_\Lambda^{(0)}$ rather than through $w \neq 0$ directly.

3. Density growth

The GDM comoving density perturbation $\Delta_g \equiv \delta_g + 3aH(1+w)\theta_g$ is related to Φ through the Einstein constraint equation $\vec{\nabla}^2 \Phi = 4\pi G \bar{\rho}_g^{(0)} a^{-1-3w} \Delta_g$. The growth rate of Δ_g is

$$f \equiv \frac{d \ln(Da^{1+3w})}{d \ln a} = \Omega_g^\gamma + 3w. \quad (\text{A14})$$

We now focus on $a = 1$ such that the factor a^{-1-3w} relating potential and density growth is irrelevant. Since most of the growth happens in the late universe bins, we then expect σ_8 and w_0 to become correlated in the *var-w* and *var-wc* models. This is what we see in the middle panel of Fig. 5 and Fig. 9.

Appendix B: ECLAIR – “Ensemble of Codes for Likelihood Analysis, Inference, and Reporting”: a short description.

We present here a brief overview of the characteristics of the ECLAIR (“Ensemble of Codes for Likelihood Analysis, Inference, and Reporting”) suite of codes, used to derive all our results in the present work.

ECLAIR is at its core a Monte Carlo code written for extracting constraints on cosmological (and also nuisance) parameters. The main sampling algorithm used in the current version is the Goodman-Weare affine invariant MCMC ensemble sampling [21], and most specifically its Python implementation in the *emcee* module [which needs to be installed

before using the ECLAIR suite 20]. This method allows for a quick and almost tuning-free exploration of the full parameter space via the use of “walkers,” spreading simultaneously and updating their positions at each MCMC step by using the positions of all the other walkers. The implementation of other sampling methods, such as the powerful nested sampling approach through the MultiNest [17] algorithm, is underway and will appear in future ECLAIR releases.

ECLAIR contains interfaces and likelihood codes for several recent experiments and surveys, including all releases of the Planck likelihood, with new likelihoods being continuously added through its ongoing development. It allows for a straightforward interface to the CLASS Boltzmann code [33] for computing and retrieving cosmological quantities and observables used subsequently by the likelihood codes. In particular, it uses the convenient *classy* python wrapper of CLASS. It comes with a bundle of scripts that allow the monitoring of the Markov chain, including a visual and convenient estimator of its convergence. A robust maximizer is included for finding the best likelihood of the explored models: it relies on a combination of the simulated annealing technique and ensemble sampling to converge reliably toward the global maximum of the posterior function. ECLAIR outputs are also easily interfaceable with the popular *getdist* python module for the computation of 1D credible regions and 2D contours.

The ECLAIR suite comes with a powerful parser and all configuration is done via a simple *.ini* file, with a variety of convenient settings. As an example, the parameter (and prior) redefinition between $\{c_s^2, c_v^2\}$ and $\{c_+^2, d\}$ (described in Sec. III C) takes a simple line of code which creates on the fly an equivalence between the new MCMC parameters (c_+^2 and d) with the parameters taken as input by CLASS (c_s^2 and c_v^2). Despite all the included capabilities, potential improvements or further case-specific modifications may be easily implemented, as the main code itself is short, well-commented, and easy to “hack.” Developed specifically for the work presented in this paper, ECLAIR is nonetheless versatile and can be applied to a variety of situations; It is free to use and modify provided the present work and ECLAIR’s dedicated explanatory article [24] are cited and the license conditions fulfilled.

Appendix C: Tables of 1D constraints of model parameters and correlation matrices

We present here tables of our constraints on model parameters for a number of (sub) models and dataset combinations. In Table III, we list the parameter constraints for six dataset combinations when flat priors were used, showing the mean value of each parameter and the boundaries of the 68% and 95% credible intervals. In Table IV we focus on two datasets, PPS and PPS+Lens+BAO, and contrast *var-wc*, *var-c* and *var-w* together with an alternative choice of priors. This table also provides the best-fit values, found by maximization of the likelihood \mathcal{L}_{max} ($-\ln \mathcal{L}_{\text{max}}$ corresponds to $\chi^2/2$ in the case of a Gaussian likelihood). Table V lists the 68% and 95% credible regions for $c_{+,i}^2$ when the PPS and PPS+Lens+BAO dataset combinations were used using “nonflat priors” (see Sec. III C).

Correlation matrices when the PPS+Lens+BAO dataset combination was used are displayed in Fig.9 (*var-wc* model; cosmological and GDM parameters; flat priors) and Fig.10 (GDM parameters only; nonflat priors) respectively.

Data Parameter	PPS	PPS+Lens	PPS+BAO	PPS+HST	PPS+Lens+BAO	PPS+Lens+HST
$100\omega_b$	$2.187^{+0.018+0.035}_{-0.018-0.034}$ $2.179^{+0.022+0.043}_{-0.022-0.044}$	$2.201^{+0.016+0.032}_{-0.017-0.033}$ $2.188^{+0.022+0.042}_{-0.022-0.043}$	$2.207^{+0.016+0.032}_{-0.016-0.031}$ $2.182^{+0.023+0.045}_{-0.023-0.044}$	$2.199^{+0.017+0.034}_{-0.017-0.033}$ $2.185^{+0.022+0.044}_{-0.022-0.043}$	$2.218^{+0.015+0.030}_{-0.015-0.030}$ $2.194^{+0.021+0.041}_{-0.021-0.041}$	$2.210^{+0.017+0.032}_{-0.016-0.033}$ $2.196^{+0.020+0.039}_{-0.020-0.040}$
$\omega_g^{(0)}$	$0.1245^{+0.0020+0.0045}_{-0.0023-0.0040}$ $0.084^{+0.012+0.049}_{-0.028-0.038}$	$0.1229^{+0.0018+0.0035}_{-0.0018-0.0033}$ $0.091^{+0.015+0.045}_{-0.026-0.036}$	$0.1200^{+0.0012+0.0024}_{-0.0012-0.0024}$ $0.121^{+0.025+0.053}_{-0.032-0.049}$	$0.1223^{+0.0018+0.0038}_{-0.0020-0.0035}$ $0.073^{+0.013+0.046}_{-0.023-0.034}$	$0.1197^{+0.0016+0.0022}_{-0.0011-0.0022}$ $0.127^{+0.014+0.046}_{-0.024-0.044}$	$0.1213^{+0.0016+0.0032}_{-0.0016-0.0031}$ $0.082^{+0.015+0.046}_{-0.025-0.036}$
H_0	$65.3^{+0.85+1.6}_{-0.84-1.7}$ < 49.5 < 55.6	$66.0^{+0.74+1.4}_{-0.73-1.4}$ < 54.6 < 63.3	$67.1^{+0.51+1.0}_{-0.51-1.0}$ 69.6^{+1.9+3.6}_{-1.9-3.6}	$66.2^{+0.75+1.4}_{-0.74-1.5}$ 70.9^{+2.3+4.6}_{-2.3-4.6}	$67.33^{+0.49+0.99}_{-0.50-0.95}$ 69.3^{+1.6+3.3}_{-1.7-3.0}	$66.7^{+0.67+1.3}_{-0.67-1.4}$ 72.0^{+2.4+4.7}_{-2.3-4.6}
τ_{reio}	$0.108^{+0.018+0.036}_{-0.018-0.035}$ $0.106^{+0.018+0.034}_{-0.018-0.034}$	$0.106^{+0.015+0.032}_{-0.015-0.030}$ $0.101^{+0.019+0.037}_{-0.020-0.039}$	$0.121^{+0.017+0.034}_{-0.017-0.034}$ $0.102^{+0.022+0.042}_{-0.022-0.041}$	$0.114^{+0.018+0.036}_{-0.018-0.037}$ $0.105^{+0.021+0.039}_{-0.019-0.041}$	$0.118^{+0.014+0.030}_{-0.016-0.028}$ $0.095^{+0.019+0.039}_{-0.020-0.037}$	$0.113^{+0.016+0.032}_{-0.016-0.031}$ $0.098^{+0.020+0.038}_{-0.020-0.037}$
$\ln(10^{10}A_s)$	$3.159^{+0.035+0.070}_{-0.035-0.068}$ $3.164^{+0.037+0.070}_{-0.036-0.068}$	$3.151^{+0.029+0.060}_{-0.029-0.057}$ $3.153^{+0.039+0.075}_{-0.039-0.077}$	$3.174^{+0.034+0.067}_{-0.035-0.067}$ $3.158^{+0.044+0.084}_{-0.044-0.082}$	$3.164^{+0.036+0.071}_{-0.035-0.071}$ $3.164^{+0.043+0.079}_{-0.039-0.083}$	$3.170^{+0.029+0.059}_{-0.029-0.055}$ $3.145^{+0.038+0.076}_{-0.039-0.073}$	$3.163^{+0.030+0.061}_{-0.030-0.059}$ $3.149^{+0.038+0.074}_{-0.039-0.074}$
n_s	$0.956^{+0.0057+0.011}_{-0.0057-0.011}$ $0.963^{+0.012+0.023}_{-0.012-0.022}$	$0.958^{+0.0053+0.010}_{-0.0054-0.011}$ $0.971^{+0.011+0.022}_{-0.011-0.021}$	$0.9640^{+0.0050+0.0097}_{-0.0050-0.010}$ $0.966^{+0.011+0.022}_{-0.011-0.022}$	$0.960^{+0.0055+0.011}_{-0.0055-0.011}$ $0.969^{+0.011+0.023}_{-0.011-0.021}$	$0.9653^{+0.0044+0.0086}_{-0.0044-0.0091}$ $0.973^{+0.010+0.022}_{-0.011-0.020}$	$0.962^{+0.0050+0.010}_{-0.0050-0.010}$ $0.976^{+0.011+0.021}_{-0.011-0.020}$
w_0	$0.13^{+0.070+0.11}_{-0.047-0.13}$	$0.0998^{+0.058+0.094}_{-0.049-0.099}$	$0.000^{+0.043+0.086}_{-0.051-0.082}$	$0.103^{+0.060+0.098}_{-0.049-0.11}$	$-0.014^{+0.034+0.075}_{-0.041-0.070}$	$0.073^{+0.058+0.094}_{-0.048-0.11}$
w_2	$-0.01^{+0.054+0.11}_{-0.053-0.10}$	$0.01^{+0.056+0.11}_{-0.054-0.11}$	$0.02^{+0.054+0.11}_{-0.054-0.11}$	$0.01^{+0.051+0.10}_{-0.051-0.10}$	$0.03^{+0.057+0.11}_{-0.055-0.11}$	$0.03^{+0.057+0.11}_{-0.055-0.11}$
w_3	$-0.004^{+0.042+0.094}_{-0.050-0.085}$	$0.003^{+0.048+0.11}_{-0.055-0.094}$	$0.078^{+0.049+0.093}_{-0.050-0.094}$	$0.044^{+0.044+0.087}_{-0.045-0.090}$	$0.078^{+0.048+0.091}_{-0.047-0.093}$	$0.050^{+0.048+0.093}_{-0.048-0.096}$
w_4	$-0.075^{+0.029+0.068}_{-0.036-0.065}$	$-0.073^{+0.035+0.069}_{-0.035-0.067}$	$-0.045^{+0.031+0.071}_{-0.036-0.064}$	$-0.061^{+0.034+0.065}_{-0.033-0.063}$	$-0.057^{+0.030+0.065}_{-0.034-0.064}$	$-0.065^{+0.032+0.070}_{-0.037-0.067}$
w_5	$-0.030^{+0.019+0.036}_{-0.019-0.037}$	$-0.024^{+0.020+0.038}_{-0.020-0.040}$	$-0.017^{+0.020+0.037}_{-0.019-0.039}$	$-0.021^{+0.019+0.039}_{-0.019-0.037}$	$-0.012^{+0.020+0.039}_{-0.020-0.039}$	$-0.015^{+0.021+0.038}_{-0.019-0.040}$
w_6	$-0.020^{+0.0060+0.012}_{-0.0060-0.012}$	$-0.020^{+0.0062+0.012}_{-0.0062-0.012}$	$-0.016^{+0.0061+0.012}_{-0.0060-0.012}$	$-0.017^{+0.0062+0.012}_{-0.0061-0.012}$	$-0.017^{+0.0067+0.012}_{-0.0061-0.012}$	$-0.017^{+0.0059+0.011}_{-0.0059-0.012}$
w_7	$0.0131^{+0.0049+0.0094}_{-0.0048-0.0095}$	$0.0152^{+0.0045+0.0089}_{-0.0046-0.0092}$	$0.0141^{+0.0045+0.0094}_{-0.0046-0.0094}$	$0.0137^{+0.0047+0.0091}_{-0.0046-0.0093}$	$0.0162^{+0.0046+0.0087}_{-0.0046-0.0088}$	$0.0153^{+0.0046+0.0083}_{-0.0046-0.0088}$
w_8	$0.070^{+0.026+0.076}_{-0.041-0.066}$	$0.089^{+0.029+0.084}_{-0.046-0.070}$	$0.069^{+0.026+0.077}_{-0.040-0.066}$	$0.075^{+0.027+0.077}_{-0.042-0.065}$	$0.090^{+0.029+0.086}_{-0.047-0.070}$	$0.091^{+0.028+0.082}_{-0.044-0.067}$
$c_{s,0}^2$	$< 1.08 \cdot 10^{-5} < 3.04 \cdot 10^{-5}$ $< 1.10 \cdot 10^{-5} < 2.99 \cdot 10^{-5}$	$< 7.46 \cdot 10^{-6} < 1.97 \cdot 10^{-5}$ $< 2.29 \cdot 10^{-5} < 6.11 \cdot 10^{-5}$	$< 1.02 \cdot 10^{-5} < 2.71 \cdot 10^{-5}$ $< 1.42 \cdot 10^{-5} < 4.04 \cdot 10^{-5}$	$< 9.75 \cdot 10^{-6} < 2.81 \cdot 10^{-5}$ $< 1.35 \cdot 10^{-5} < 4.06 \cdot 10^{-5}$	$< 6.23 \cdot 10^{-6} < 1.61 \cdot 10^{-5}$ $< 1.51 \cdot 10^{-5} < 3.99 \cdot 10^{-5}$	$< 7.46 \cdot 10^{-6} < 2.07 \cdot 10^{-5}$ $< 2.15 \cdot 10^{-5} < 5.47 \cdot 10^{-5}$
$c_{s,1}^2$	$< 3.76 \cdot 10^{-6} < 9.65 \cdot 10^{-6}$ $< 6.61 \cdot 10^{-6} < 1.76 \cdot 10^{-5}$	$< 1.38 \cdot 10^{-6} < 3.75 \cdot 10^{-6}$ $< 2.19 \cdot 10^{-6} < 5.85 \cdot 10^{-6}$	$< 3.35 \cdot 10^{-6} < 8.92 \cdot 10^{-6}$ $< 4.38 \cdot 10^{-6} < 1.12 \cdot 10^{-5}$	$< 3.50 \cdot 10^{-6} < 9.21 \cdot 10^{-6}$ $< 4.53 \cdot 10^{-6} < 1.22 \cdot 10^{-5}$	$< 1.24 \cdot 10^{-6} < 3.41 \cdot 10^{-6}$ $< 1.68 \cdot 10^{-6} < 4.51 \cdot 10^{-6}$	$< 1.25 \cdot 10^{-6} < 3.34 \cdot 10^{-6}$ $< 1.95 \cdot 10^{-6} < 5.74 \cdot 10^{-6}$
$c_{s,2}^2$	$< 7.04 \cdot 10^{-6} < 1.87 \cdot 10^{-5}$ $< 1.67 \cdot 10^{-5} < 4.32 \cdot 10^{-5}$	$< 2.32 \cdot 10^{-6} < 6.22 \cdot 10^{-6}$ $< 4.48 \cdot 10^{-6} < 1.08 \cdot 10^{-5}$	$< 6.35 \cdot 10^{-6} < 1.63 \cdot 10^{-5}$ $< 8.58 \cdot 10^{-6} < 2.13 \cdot 10^{-5}$	$< 6.55 \cdot 10^{-6} < 1.74 \cdot 10^{-5}$ $< 9.95 \cdot 10^{-6} < 2.63 \cdot 10^{-5}$	$< 2.21 \cdot 10^{-6} < 5.74 \cdot 10^{-6}$ $< 2.88 \cdot 10^{-6} < 7.90 \cdot 10^{-6}$	$< 2.19 \cdot 10^{-6} < 5.56 \cdot 10^{-6}$ $< 3.60 \cdot 10^{-6} < 8.97 \cdot 10^{-6}$
$c_{s,3}^2$	$< 2.01 \cdot 10^{-5} < 5.09 \cdot 10^{-5}$ $< 4.90 \cdot 10^{-5} < 0.000124$	$< 6.35 \cdot 10^{-6} < 1.61 \cdot 10^{-5}$ $< 1.35 \cdot 10^{-5} < 3.52 \cdot 10^{-5}$	$< 1.98 \cdot 10^{-5} < 5.31 \cdot 10^{-5}$ $< 2.93 \cdot 10^{-5} < 8.54 \cdot 10^{-5}$	$< 2.03 \cdot 10^{-5} < 5.42 \cdot 10^{-5}$ $< 3.24 \cdot 10^{-5} < 9.80 \cdot 10^{-5}$	$< 6.15 \cdot 10^{-6} < 1.52 \cdot 10^{-5}$ $< 9.65 \cdot 10^{-6} < 2.43 \cdot 10^{-5}$	$< 6.28 \cdot 10^{-6} < 1.62 \cdot 10^{-5}$ $< 1.07 \cdot 10^{-5} < 3.12 \cdot 10^{-5}$
$c_{s,4}^2$	$< 6.75 \cdot 10^{-5} < 0.000184$ $< 0.000131 < 0.000336$	$< 2.09 \cdot 10^{-5} < 5.50 \cdot 10^{-5}$ $< 3.21 \cdot 10^{-5} < 8.15 \cdot 10^{-5}$	$< 5.68 \cdot 10^{-5} < 0.000147$ $< 8.37 \cdot 10^{-5} < 0.000219$	$< 6.06 \cdot 10^{-5} < 0.000169$ $< 0.000102 < 0.000254$	$< 1.94 \cdot 10^{-5} < 5.13 \cdot 10^{-5}$ $< 2.83 \cdot 10^{-5} < 6.92 \cdot 10^{-5}$	$< 1.90 \cdot 10^{-5} < 4.96 \cdot 10^{-5}$ $< 3.04 \cdot 10^{-5} < 8.22 \cdot 10^{-5}$
$c_{s,5}^2$	$< 0.000215 < 0.000580$ $< 0.000264 < 0.000679$	$< 6.23 \cdot 10^{-5} < 0.000161$ $< 9.52 \cdot 10^{-5} < 0.000238$	$< 0.000199 < 0.000541$ $< 0.000244 < 0.000685$	$< 0.000209 < 0.000548$ $< 0.000248 < 0.000700$	$< 5.31 \cdot 10^{-5} < 0.000134$ $< 7.36 \cdot 10^{-5} < 0.000194$	$< 5.90 \cdot 10^{-5} < 0.000145$ $< 8.06 \cdot 10^{-5} < 0.000210$
$c_{s,6}^2$	$< 0.000952 < 0.00142$ $< 0.000567 < 0.00112$	$< 0.000350 < 0.000735$ $< 0.000239 < 0.000534$	$< 0.000663 < 0.00119$ $< 0.000456 < 0.000927$	$< 0.000783 < 0.00132$ $< 0.000481 < 0.000992$	$< 0.000317 < 0.000631$ $< 0.000197 < 0.000476$	$< 0.000326 < 0.000672$ $< 0.000199 < 0.000511$
$c_{s,7}^2$	$< 0.00223 < 0.00387$ $< 0.00200 < 0.00382$	$< 0.00131 < 0.00256$ $< 0.00133 < 0.00276$	$< 0.00174 < 0.00325$ $< 0.00193 < 0.00363$	$< 0.00212 < 0.00383$ $< 0.00198 < 0.00378$	$< 0.000883 < 0.00187$ $< 0.00132 < 0.00261$	$< 0.00114 < 0.00233$ $< 0.00139 < 0.00287$
$c_{s,8}^2$	$< 0.00501 < 0.0113$ $< 0.0247 < 0.0503$	$< 0.00380 < 0.00896$ $< 0.0311 < 0.0587$	$< 0.00469 < 0.0110$ $< 0.0243 < 0.0503$	$< 0.00524 < 0.0120$ $< 0.0250 < 0.0497$	$< 0.00304 < 0.00714$ $< 0.0318 < 0.0589$	$< 0.00348 < 0.00841$ $< 0.0304 < 0.0580$
$c_{\text{vis},0}^2$	$< 4.10 \cdot 10^{-5} < 0.000124$ $< 4.64 \cdot 10^{-5} < 0.000152$	$< 4.16 \cdot 10^{-5} < 0.000128$ $< 0.000321 < 0.000701$	$< 3.72 \cdot 10^{-5} < 0.000113$ $< 5.53 \cdot 10^{-5} < 0.000198$	$< 4.07 \cdot 10^{-5} < 0.000127$ $< 7.70 \cdot 10^{-5} < 0.000253$	$< 3.26 \cdot 10^{-5} < 0.000114$ $< 0.000104 < 0.000355$	$< 3.90 \cdot 10^{-5} < 0.000137$ $< 0.000180 < 0.000474$
$c_{\text{vis},1}^2$	$< 6.00 \cdot 10^{-6} < 1.62 \cdot 10^{-5}$ $< 1.18 \cdot 10^{-5} < 3.06 \cdot 10^{-5}$	$< 2.34 \cdot 10^{-6} < 6.40 \cdot 10^{-6}$ $< 4.92 \cdot 10^{-6} < 1.34 \cdot 10^{-5}$	$< 5.57 \cdot 10^{-6} < 1.49 \cdot 10^{-5}$ $< 7.27 \cdot 10^{-6} < 2.14 \cdot 10^{-5}$	$< 5.81 \cdot 10^{-6} < 1.46 \cdot 10^{-5}$ $< 9.12 \cdot 10^{-6} < 2.41 \cdot 10^{-5}$	$< 2.22 \cdot 10^{-6} < 5.73 \cdot 10^{-6}$ $< 3.78 \cdot 10^{-6} < 1.00 \cdot 10^{-5}$	$< 2.50 \cdot 10^{-6} < 7.20 \cdot 10^{-6}$ $< 4.11 \cdot 10^{-6} < 1.22 \cdot 10^{-5}$
$c_{\text{vis},2}^2$	$< 9.11 \cdot 10^{-6} < 2.70 \cdot 10^{-5}$ $< 2.18 \cdot 10^{-5} < 5.78 \cdot 10^{-5}$	$< 3.06 \cdot 10^{-6} < 8.05 \cdot 10^{-6}$ $< 5.95 \cdot 10^{-6} < 1.57 \cdot 10^{-5}$	$< 7.97 \cdot 10^{-6} < 2.13 \cdot 10^{-5}$ $< 1.11 \cdot 10^{-5} < 3.01 \cdot 10^{-5}$	$< 7.84 \cdot 10^{-6} < 1.98 \cdot 10^{-5}$ $< 1.34 \cdot 10^{-5} < 3.51 \cdot 10^{-5}$	$< 2.88 \cdot 10^{-6} < 7.73 \cdot 10^{-6}$ $< 4.36 \cdot 10^{-6} < 1.08 \cdot 10^{-5}$	$< 2.98 \cdot 10^{-6} < 7.75 \cdot 10^{-6}$ $< 4.55 \cdot 10^{-6} < 1.24 \cdot 10^{-5}$
$c_{\text{vis},3}^2$	$< 2.51 \cdot 10^{-5} < 6.99 \cdot 10^{-5}$ $< 5.88 \cdot 10^{-5} < 0.000152$	$< 8.09 \cdot 10^{-6} < 2.19 \cdot 10^{-5}$ $< 1.37 \cdot 10^{-5} < 3.57 \cdot 10^{-5}$	$< 2.20 \cdot 10^{-5} < 6.26 \cdot 10^{-5}$ $< 3.58 \cdot 10^{-5} < 9.26 \cdot 10^{-5}$	$< 2.43 \cdot 10^{-5} < 6.20 \cdot 10^{-5}$ $< 4.16 \cdot 10^{-5} < 0.000105$	$< 7.28 \cdot 10^{-6} < 1.88 \cdot 10^{-5}$ $< 1.28 \cdot 10^{-5} < 3.30 \cdot 10^{-5}$	$< 8.09 \cdot 10^{-6} < 2.13 \cdot 10^{-5}$ $< 1.25 \cdot 10^{-5} < 3.33 \cdot 10^{-5}$
$c_{\text{vis},4}^2$	$< 8.17 \cdot 10^{-5} < 0.000231$ $< 0.000152 < 0.000395$	$< 2.43 \cdot 10^{-5} < 6.58 \cdot 10^{-5}$ $< 3.79 \cdot 10^{-5} < 0.000101$	$< 6.84 \cdot 10^{-5} < 0.000177$ $< 0.000100 < 0.000276$	$< 7.61 \cdot 10^{-5} < 0.000208$ $< 0.000115 < 0.000332$	$< 2.39 \cdot 10^{-5} < 6.10 \cdot 10^{-5}$ $< 3.27 \cdot 10^{-5} < 8.09 \cdot 10^{-5}$	$< 2.40 \cdot 10^{-5} < 6.19 \cdot 10^{-5}$ $< 3.49 \cdot 10^{-5} < 9.30 \cdot 10^{-5}$
$c_{\text{vis},5}^2$	$< 0.000273 < 0.000765$ $< 0.000377 < 0.000988$	$< 8.37 \cdot 10^{-5} < 0.000223$ $< 0.000101 < 0.000278$	$< 0.000263 < 0.000722$ $< 0.000292 < 0.000821$	$< 0.000273 < 0.000744$ $< 0.000333 < 0.000952$	$< 8.01 \cdot 10^{-5} < 0.000209$ $< 0.000102 < 0.000267$	$< 7.94 \cdot 10^{-5} < 0.000215$ $< 0.000104 < 0.000269$
$c_{\text{vis},6}^2$	$< 0.000786 < 0.00172$ $< 0.000622 < 0.00146$	$< 0.000364 < 0.000811$ $< 0.000292 < 0.000640$	$< 0.000798 < 0.00167$ $< 0.000514 < 0.00124$	$< 0.000786 < 0.00166$ $< 0.000549 < 0.00128$	$< 0.000356 < 0.000823$ $< 0.000253 < 0.000591$	$< 0.000361 < 0.000853$ $< 0.000255 < 0.000637$

Parameter $-\ln(\mathcal{L}_{\max})$	PPS			PPS+Lens+BAO		
	var-c:6467.722, var-wc:6462.443, var-w:6462.040, Λ CDM:6467.585			6475.377, 6471.250, 6470.89, 6475.238		
	flat prior on $c_{s,i}^2, c_{vis,i}^2$	nonflat prior on $c_{s,i}^2, c_{vis,i}^2$	best fit	flat prior on $c_{s,i}^2, c_{vis,i}^2$	nonflat prior on $c_{s,i}^2, c_{vis,i}^2$	best fit
w_0	0.13 ^{+0.070 +0.11} _{-0.047 -0.13} -0.01 ^{+0.080 +0.15} _{-0.084 -0.15}	0.133 ^{+0.052 +0.12} _{-0.052 -0.090}	0.1139 -0.007	-0.014 ^{+0.034 +0.075} _{-0.041 -0.070} -0.070 ^{+0.039 +0.088} _{-0.047 -0.087}	-0.022 ^{+0.028 +0.088} _{-0.048 -0.065}	-0.0558 -0.072
w_2	-0.01 ^{+0.054 +0.11} _{-0.053 -0.10} 0.00 ^{+0.060 +0.13} _{-0.065 -0.12}	-0.02 ^{+0.047 +0.10} _{-0.055 -0.10}	-0.0092 0.0209	0.03 ^{+0.057 +0.11} _{-0.056 -0.11} 0.03 ^{+0.065 +0.12} _{-0.065 -0.12}	0.03 ^{+0.056 +0.12} _{-0.066 -0.11}	0.0361 0.0342
w_3	-0.004 ^{+0.042 +0.094} _{-0.050 -0.085} 0.02 ^{+0.057 +0.12} _{-0.068 -0.11}	-0.015 ^{+0.041 +0.10} _{-0.052 -0.085}	-0.0450 -0.002	0.078 ^{+0.048 +0.091} _{-0.047 -0.093} 0.05 ^{+0.054 +0.10} _{-0.054 -0.10}	0.064 ^{+0.050 +0.095} _{-0.051 -0.096}	0.0498 0.0521
w_4	-0.075 ^{+0.029 +0.068} _{-0.036 -0.065} -0.047 ^{+0.034 +0.068} _{-0.034 -0.066}	-0.068 ^{+0.030 +0.069} _{-0.035 -0.066}	-0.0643 -0.0533	-0.057 ^{+0.030 +0.065} _{-0.034 -0.064} -0.037 ^{+0.033 +0.073} _{-0.039 -0.070}	-0.051 ^{+0.030 +0.070} _{-0.036 -0.063}	-0.0512 -0.0467
w_5	-0.030 ^{+0.019 +0.036} _{-0.019 -0.037} 0.002 ^{+0.020 +0.036} _{-0.018 -0.040}	-0.024 ^{+0.020 +0.037} _{-0.019 -0.038}	-0.00691 0.0041	-0.012 ^{+0.020 +0.039} _{-0.020 -0.039} 0.007 ^{+0.019 +0.038} _{-0.019 -0.039}	-0.003 ^{+0.019 +0.038} _{-0.019 -0.038}	0.00988 0.0110
w_6	-0.020 ^{+0.060 +0.012} _{-0.060 -0.012} -0.0066 ^{+0.0051 +0.0098} _{-0.0052 -0.0095}	-0.017 ^{+0.0067 +0.012} _{-0.0057 -0.012}	-0.00887 -0.00788	-0.017 ^{+0.0067 +0.012} _{-0.0062 -0.013} -0.0034 ^{+0.0049 +0.0096} _{-0.0048 -0.0094}	-0.012 ^{+0.0063 +0.012} _{-0.0062 -0.013}	-0.00466 -0.00391
w_7	0.0131 ^{+0.0049 +0.0094} _{-0.0048 -0.0095} 0.0084 ^{+0.0040 +0.0080} _{-0.0040 -0.0082}	0.0123 ^{+0.0046 +0.0091} _{-0.0047 -0.0095}	0.00803 -0.00788	0.0162 ^{+0.0047 +0.0087} _{-0.0046 -0.0088} 0.0078 ^{+0.0039 +0.0077} _{-0.0039 -0.0078}	0.0137 ^{+0.0047 +0.0089} _{-0.0042 -0.0086}	0.00930 0.00852
w_8	0.070 ^{+0.026 +0.076} _{-0.041 -0.066} 0.020 ^{+0.016 +0.033} _{-0.016 -0.031}	0.059 ^{+0.022 +0.068} _{-0.037 -0.059}	0.01863 0.0113	0.090 ^{+0.029 +0.086} _{-0.047 -0.070} 0.016 ^{+0.015 +0.029} _{-0.015 -0.030}	0.062 ^{+0.019 +0.082} _{-0.038 -0.061}	0.0143 0.0123
$c_{s,0}^2$	< 1.08 · 10 ⁻⁵ < 3.04 · 10 ⁻⁵ < 1.10 · 10 ⁻⁵ < 2.99 · 10 ⁻⁵	< 4.36 · 10 ⁻⁶ < 1.63 · 10 ⁻⁵ < 6.46 · 10 ⁻⁶ < 2.23 · 10 ⁻⁵	< 4.43 · 10 ⁻⁸ < 1.36 · 10 ⁻⁷	< 6.23 · 10 ⁻⁶ < 1.61 · 10 ⁻⁵ < 1.51 · 10 ⁻⁵ < 4.00 · 10 ⁻⁵	< 2.94 · 10 ⁻⁶ < 1.06 · 10 ⁻⁵ < 7.09 · 10 ⁻⁶ < 2.65 · 10 ⁻⁵	< 3.03 · 10 ⁻⁸ < 9.68 · 10 ⁻⁸
$c_{s,1}^2$	< 3.76 · 10 ⁻⁶ < 9.65 · 10 ⁻⁶ < 6.61 · 10 ⁻⁶ < 1.76 · 10 ⁻⁵	< 1.34 · 10 ⁻⁶ < 5.14 · 10 ⁻⁶ < 3.61 · 10 ⁻⁶ < 1.24 · 10 ⁻⁵	< 1.71 · 10 ⁻⁸ < 1.35 · 10 ⁻⁷	< 1.24 · 10 ⁻⁶ < 3.41 · 10 ⁻⁶ < 1.68 · 10 ⁻⁶ < 4.52 · 10 ⁻⁶	< 5.28 · 10 ⁻⁷ < 1.93 · 10 ⁻⁶ < 8.41 · 10 ⁻⁷ < 3.15 · 10 ⁻⁶	< 1.71 · 10 ⁻⁸ < 2.83 · 10 ⁻⁸
$c_{s,2}^2$	< 7.04 · 10 ⁻⁶ < 1.87 · 10 ⁻⁵ < 1.67 · 10 ⁻⁵ < 4.32 · 10 ⁻⁵	< 2.93 · 10 ⁻⁶ < 1.11 · 10 ⁻⁵ < 7.98 · 10 ⁻⁶ < 3.48 · 10 ⁻⁵	3.4 · 10 ⁻⁸ 4.8 · 10 ⁻⁷	< 2.21 · 10 ⁻⁶ < 5.74 · 10 ⁻⁶ < 2.88 · 10 ⁻⁶ < 7.90 · 10 ⁻⁶	< 1.00 · 10 ⁻⁶ < 3.71 · 10 ⁻⁶ < 1.41 · 10 ⁻⁶ < 5.29 · 10 ⁻⁶	4.6 · 10 ⁻⁸ < 1.19 · 10 ⁻⁷
$c_{s,3}^2$	< 2.01 · 10 ⁻⁵ < 5.09 · 10 ⁻⁵ < 4.90 · 10 ⁻⁵ < 0.000124	< 8.00 · 10 ⁻⁶ < 2.89 · 10 ⁻⁵ < 2.48 · 10 ⁻⁵ < 8.89 · 10 ⁻⁵	1.2 · 10 ⁻⁷ < 1.19 · 10 ⁻⁶	< 6.15 · 10 ⁻⁶ < 1.52 · 10 ⁻⁵ < 9.63 · 10 ⁻⁶ < 2.43 · 10 ⁻⁵	< 3.07 · 10 ⁻⁶ < 1.12 · 10 ⁻⁵ < 4.61 · 10 ⁻⁶ < 1.48 · 10 ⁻⁵	< 1.00 · 10 ⁻⁷ 2.2 · 10 ⁻⁷
$c_{s,4}^2$	< 6.75 · 10 ⁻⁵ < 0.000184 < 0.000131 < 0.000336	< 2.50 · 10 ⁻⁵ < 9.70 · 10 ⁻⁵ < 6.34 · 10 ⁻⁵ < 0.000257	0.52 · 10 ⁻⁷ 3.1 · 10 ⁻⁶	< 1.94 · 10 ⁻⁵ < 5.13 · 10 ⁻⁵ < 2.83 · 10 ⁻⁵ < 6.92 · 10 ⁻⁵	< 8.51 · 10 ⁻⁶ < 3.07 · 10 ⁻⁵ < 1.39 · 10 ⁻⁵ < 4.84 · 10 ⁻⁵	< 3.38 · 10 ⁻⁷ < 7.92 · 10 ⁻⁷
$c_{s,5}^2$	< 0.000215 < 0.000580 < 0.000264 < 0.000679	< 7.23 · 10 ⁻⁵ < 0.000271 < 0.000157 < 0.000554	1.6 · 10 ⁻⁶ < 4.09 · 10 ⁻⁶	< 5.31 · 10 ⁻⁵ < 0.000134 < 7.36 · 10 ⁻⁵ < 0.000193	< 2.55 · 10 ⁻⁵ < 8.89 · 10 ⁻⁵ < 4.03 · 10 ⁻⁵ < 0.000152	< 7.43 · 10 ⁻⁷ < 1.79 · 10 ⁻⁶
$c_{s,6}^2$	< 0.000952 < 0.00142 < 0.000567 < 0.00112	< 0.000498 < 0.00100 < 0.000334 < 0.000889	0.000142 0.000367	< 0.000317 < 0.000631 < 0.000197 < 0.000477	< 0.000164 < 0.000450 < 9.69 · 10 ⁻⁵ < 0.000326	8.4 · 10 ⁻⁵ < 1.08 · 10 ⁻⁵
$c_{s,7}^2$	< 0.00223 < 0.00387 < 0.00200 < 0.00382	< 0.00137 < 0.00304 < 0.00150 < 0.00307	4.0 · 10 ⁻⁵ 0.000920	< 0.000883 < 0.00187 < 0.00132 < 0.00261	< 0.000358 < 0.00117 < 0.000725 < 0.00195	0.81 · 10 ⁻⁵ 6.18 · 10 ⁻⁵
$c_{s,8}^2$	< 0.00501 < 0.0113 < 0.0247 < 0.0503	< 0.00246 < 0.00725 < 0.0168 < 0.0424	6.9 · 10 ⁻⁵ 0.00026	< 0.00304 < 0.00714 < 0.0318 < 0.0589	< 0.00168 < 0.00602 < 0.0156 < 0.0469	< 6.93 · 10 ⁻⁵ < 0.000576
$c_{vis,0}^2$	< 4.10 · 10 ⁻⁵ < 0.000124 < 4.64 · 10 ⁻⁵ < 0.000152	< 1.21 · 10 ⁻⁵ < 5.82 · 10 ⁻⁵ < 2.09 · 10 ⁻⁵ < 0.000101	< 9.68 · 10 ⁻⁸ < 7.50 · 10 ⁻⁷	< 3.26 · 10 ⁻⁵ < 0.000114 < 0.000104 < 0.000355	< 8.95 · 10 ⁻⁶ < 4.46 · 10 ⁻⁵ < 3.34 · 10 ⁻⁵ < 0.000223	< 3.13 · 10 ⁻⁸ < 3.75 · 10 ⁻⁷
$c_{vis,1}^2$	< 6.00 · 10 ⁻⁶ < 1.62 · 10 ⁻⁵ < 1.18 · 10 ⁻⁵ < 3.06 · 10 ⁻⁵	< 2.57 · 10 ⁻⁶ < 8.89 · 10 ⁻⁶ < 6.30 · 10 ⁻⁶ < 2.28 · 10 ⁻⁵	< 3.12 · 10 ⁻⁸ 2.3 · 10 ⁻⁷	< 2.22 · 10 ⁻⁶ < 5.73 · 10 ⁻⁶ < 3.78 · 10 ⁻⁶ < 1.00 · 10 ⁻⁵	< 9.74 · 10 ⁻⁷ < 3.34 · 10 ⁻⁶ < 1.74 · 10 ⁻⁶ < 6.20 · 10 ⁻⁶	1.9 · 10 ⁻⁸ < 5.07 · 10 ⁻⁸
$c_{vis,2}^2$	< 9.11 · 10 ⁻⁶ < 2.70 · 10 ⁻⁵ < 2.18 · 10 ⁻⁵ < 5.78 · 10 ⁻⁵	< 4.12 · 10 ⁻⁶ < 1.45 · 10 ⁻⁵ < 1.11 · 10 ⁻⁵ < 4.21 · 10 ⁻⁵	0.67 · 10 ⁻⁸ 0.80 · 10 ⁻⁶	< 2.88 · 10 ⁻⁶ < 7.73 · 10 ⁻⁶ < 4.35 · 10 ⁻⁶ < 1.08 · 10 ⁻⁵	< 1.51 · 10 ⁻⁶ < 5.09 · 10 ⁻⁶ < 2.19 · 10 ⁻⁶ < 7.92 · 10 ⁻⁶	< 3.26 · 10 ⁻⁸ < 5.95 · 10 ⁻⁸
$c_{vis,3}^2$	< 2.51 · 10 ⁻⁵ < 6.99 · 10 ⁻⁵ < 5.88 · 10 ⁻⁵ < 0.000152	< 1.13 · 10 ⁻⁵ < 4.11 · 10 ⁻⁵ < 3.33 · 10 ⁻⁵ < 0.000104	1.7 · 10 ⁻⁷ < 1.78 · 10 ⁻⁶	< 7.28 · 10 ⁻⁶ < 1.88 · 10 ⁻⁵ < 1.28 · 10 ⁻⁵ < 3.30 · 10 ⁻⁵	< 4.14 · 10 ⁻⁶ < 1.29 · 10 ⁻⁵ < 7.01 · 10 ⁻⁶ < 2.24 · 10 ⁻⁵	< 1.60 · 10 ⁻⁷ 5.6 · 10 ⁻⁷
$c_{vis,4}^2$	< 8.17 · 10 ⁻⁵ < 0.000231 < 0.000152 < 0.000395	< 3.81 · 10 ⁻⁵ < 0.000128 < 8.02 · 10 ⁻⁵ < 0.000280	< 3.86 · 10 ⁻⁷ 4.8 · 10 ⁻⁶	< 2.39 · 10 ⁻⁵ < 6.10 · 10 ⁻⁵ < 3.27 · 10 ⁻⁵ < 8.09 · 10 ⁻⁵	< 1.27 · 10 ⁻⁵ < 4.30 · 10 ⁻⁵ < 1.88 · 10 ⁻⁵ < 6.41 · 10 ⁻⁵	< 2.18 · 10 ⁻⁷ 1.2 · 10 ⁻⁶
$c_{vis,5}^2$	< 0.000273 < 0.000765 < 0.000377 < 0.000988	< 0.000119 < 0.000406 < 0.000252 < 0.000760	< 2.09 · 10 ⁻⁶ < 6.69 · 10 ⁻⁶	< 8.01 · 10 ⁻⁵ < 0.000209 < 0.000102 < 0.000267	< 3.99 · 10 ⁻⁵ < 0.000130 < 6.29 · 10 ⁻⁵ < 0.000205	< 1.30 · 10 ⁻⁶ 0.66 · 10 ⁻⁶
$c_{vis,6}^2$	< 0.000786 < 0.00172 < 0.000622 < 0.00146	< 0.000511 < 0.00122 < 0.000412 < 0.00115	1.5 · 10 ⁻⁵ < 3.52 · 10 ⁻⁵	< 0.000356 < 0.000823 < 0.000253 < 0.000590	< 0.000222 < 0.000604 < 0.000148 < 0.000470	< 1.74 · 10 ⁻⁵ 0.98 · 10 ⁻⁵
$c_{vis,7}^2$	< 0.00660 < 0.0102 < 0.00764 < 0.0133	< 0.00331 < 0.00717 < 0.00539 < 0.0115	< 5.62 · 10 ⁻⁵ 0.00319	< 0.00107 < 0.00252 < 0.00267 < 0.00596	< 0.000549 < 0.00163 < 0.00161 < 0.00491	< 2.49 · 10 ⁻⁵ 7.8 · 10 ⁻⁵
$c_{vis,8}^2$	< 0.00681 < 0.0159 < 0.0212 < 0.0452	< 0.00382 < 0.0118 < 0.0154 < 0.0390	0.000101 < 0.000659	< 0.00478 < 0.0114 < 0.0211 < 0.0455	< 0.00253 < 0.00839 < 0.0143 < 0.0347	< 3.61 · 10 ⁻⁵ 0.00049
σ_8	0.278 ^{+0.041 +0.091} _{-0.047 -0.081} 0.41 ^{+0.084 +0.18} _{-0.10 -0.18} 0.76 ^{+0.18 +0.50} _{-0.29 -0.41}	0.39 ^{+0.066 +0.13} _{-0.067 -0.12} 0.50 ^{+0.098 +0.22} _{-0.12 -0.21}	0.778 0.829 0.71	0.386 ^{+0.049 +0.11} _{-0.061 -0.099} 0.32 ^{+0.051 +0.13} _{-0.070 -0.12} 0.68 ^{+0.084 +0.30} _{-0.15 -0.25}	0.49 ^{+0.090 +0.14} _{-0.071 -0.15} 0.39 ^{+0.065 +0.18} _{-0.11 -0.16}	0.7868 0.659 0.656

TABLE IV. Constraints on the var-c/var-wc/var-w (Black/blue/green respectively) parameters when two dataset combinations (PPS and PPS+lens+BAO) and both types of priors were used. The upper and lower limits of the 68% and 95% credible regions around the mean are shown. The maximum likelihood $-\ln \mathcal{L}_{\max}$ is stated in the first row; Λ CDM value in grey.

Parameter	PPS		PPS+Lens+BAO	
	68% and 95% C.L.	best fit	68% and 95% C.L.	best fit
$c_{+,0}^2$	$< 1.19 \cdot 10^{-5} < 4.14 \cdot 10^{-5}$ $< 1.94 \cdot 10^{-5} < 6.58 \cdot 10^{-5}$	$0.71 \cdot 10^{-7}$ $3.8 \cdot 10^{-7}$	$< 8.53 \cdot 10^{-6} < 3.03 \cdot 10^{-5}$ $< 2.65 \cdot 10^{-5} < 0.000139$	$< 5.48 \cdot 10^{-8}$ $< 3.14 \cdot 10^{-7}$
$c_{+,1}^2$	$< 3.03 \cdot 10^{-6} < 8.19 \cdot 10^{-6}$ $< 7.80 \cdot 10^{-6} < 1.99 \cdot 10^{-5}$	$2.5 \cdot 10^{-8}$ $2.3 \cdot 10^{-7}$	$< 1.14 \cdot 10^{-6} < 3.11 \cdot 10^{-6}$ $< 2.01 \cdot 10^{-6} < 5.44 \cdot 10^{-6}$	$2.3 \cdot 10^{-8}$ $4.0 \cdot 10^{-8}$
$c_{+,2}^2$	$< 5.72 \cdot 10^{-6} < 1.61 \cdot 10^{-5}$ $< 1.53 \cdot 10^{-5} < 4.90 \cdot 10^{-5}$	$0.70 \cdot 10^{-8}$ $0.91 \cdot 10^{-6}$	$< 2.04 \cdot 10^{-6} < 5.44 \cdot 10^{-6}$ $< 2.84 \cdot 10^{-6} < 8.06 \cdot 10^{-6}$	$0.60 \cdot 10^{-8}$ $1.09 \cdot 10^{-7}$
$c_{+,3}^2$	$< 1.57 \cdot 10^{-3} < 4.29 \cdot 10^{-3}$ $< 4.81 \cdot 10^{-5} < 0.000120$	$2.1 \cdot 10^{-7}$ $1.6 \cdot 10^{-6}$	$< 5.90 \cdot 10^{-6} < 1.53 \cdot 10^{-5}$ $< 9.09 \cdot 10^{-6} < 2.39 \cdot 10^{-5}$	$1.4 \cdot 10^{-7}$ $5.2 \cdot 10^{-7}$
$c_{+,4}^2$	$< 5.06 \cdot 10^{-5} < 0.000141$ $< 0.000119 < 0.000348$	$0.68 \cdot 10^{-6}$ $5.6 \cdot 10^{-6}$	$< 1.70 \cdot 10^{-5} < 4.60 \cdot 10^{-5}$ $< 2.63 \cdot 10^{-5} < 6.81 \cdot 10^{-5}$	$3.6 \cdot 10^{-7}$ $1.26 \cdot 10^{-6}$
$c_{+,5}^2$	$< 0.000151 < 0.000411$ $< 0.000321 < 0.000829$	$2.4 \cdot 10^{-6}$ $0.57 \cdot 10^{-6}$	$< 5.23 \cdot 10^{-5} < 0.000132$ $< 8.20 \cdot 10^{-5} < 0.000223$	$1.13 \cdot 10^{-6}$ $5.1 \cdot 10^{-6}$
$c_{+,6}^2$	$< 0.000883 < 0.00129$ $< 0.000588 < 0.00118$	0.000150 0.000381	$< 0.000299 < 0.000602$ $< 0.000195 < 0.000478$	0.000090 $1.30 \cdot 10^{-5}$
$c_{+,7}^2$	$< 0.00338 < 0.00545$ $< 0.00474 < 0.00737$	0.000063 0.002619	$< 0.000708 < 0.00168$ $< 0.00169 < 0.00369$	$1.8 \cdot 10^{-5}$ 0.000103
$c_{+,8}^2$	$< 0.00497 < 0.0110$ $< 0.0262 < 0.0505$	0.000123 0.00051	$< 0.00338 < 0.00867$ $< 0.0242 < 0.0534$	$< 9.08 \cdot 10^{-5}$ 0.00064

TABLE V. The 68% and 95% credible regions for $c_{+,i}^2$ when the PPS and PPS+Lens+BAO dataset combinations were used using “nonflat priors” (see Sec. III C). Black/blue fonts show constraints for var-c/var-wc, respectively.

	w_0	w_2	w_3	w_4	w_5	w_6	w_7	w_8	$c_{s,0}^2$	$c_{s,1}^2$	$c_{s,2}^2$	$c_{s,3}^2$	$c_{s,4}^2$	$c_{s,5}^2$	$c_{s,6}^2$	$c_{s,7}^2$	$c_{s,8}^2$	$c_{vis,0}^2$	$c_{vis,1}^2$	$c_{vis,2}^2$	$c_{vis,3}^2$	$c_{vis,4}^2$	$c_{vis,5}^2$	$c_{vis,6}^2$	$c_{vis,7}^2$	$c_{vis,8}^2$	ω_b	$\omega_b^{(0)}$	H_0	τ_{reio}	$\ln(10^{10} A_s)$	n_s	σ_8
ω_b	11.3	-12.4	-12.5	-7.3	43.6	5.0	-17.6	27.8	-13.6	-0.7	-2.8	-4.7	-4.9	-7.9	-12.3	5.3	16.4	-12.0	-4.4	-9.9	-4.7	-0.7	-2.6	-5.0	0.5	-0.1							
$\omega_b^{(0)}$	-96.8	7.9	23.6	13.3	-5.0	-9.5	-1.0	3.3	-4.9	-3.3	-7.8	-1.3	-3.3	-0.3	-0.0	-0.1	2.6	-17.1	-7.0	-7.2	1.6	-6.0	-9.1	-4.0	0.4	3.3	-8.3						
H_0	75.5	8.4	-18.3	-18.5	1.0	-18.0	12.4	16.2	6.3	1.0	6.8	7.7	3.7	2.7	-2.8	5.8	14.7	17.2	6.1	9.7	4.1	7.2	8.4	2.5	4.8	2.8	3.7	-80.8					
τ_{reio}	14.1	-39.8	5.2	20.7	10.0	31.6	-12.1	-4.2	25.3	14.0	8.6	-3.5	2.8	2.3	0.6	2.3	-10.0	32.4	12.3	-0.4	-1.7	4.9	5.3	5.0	2.0	-4.7	21.9	-7.3	-12.5				
$\ln(10^{10} A_s)$	14.3	-39.0	3.7	18.2	17.0	28.9	-2.2	-1.7	28.5	15.5	10.0	-1.7	4.1	2.7	-0.9	6.0	-11.2	35.4	13.9	0.2	-1.2	5.4	6.7	4.6	7.2	0.9	19.9	-6.6	-10.0	97.3			
n_s	10.3	-2.8	8.9	-34.0	14.7	30.9	17.6	21.2	-3.0	3.7	1.6	0.3	-4.3	-4.2	-17.8	11.4	-6.4	0.9	-0.0	0.6	-0.6	2.0	3.5	-10.0	10.7	14.4	36.0	-12.0	-1.4	41.4	43.0		
σ_8	58.5	3.3	-22.4	-18.4	15.2	20.4	-9.3	-11.9	-51.3	-4.9	1.8	-3.8	-4.0	-3.9	-7.3	-6.3	-9.9	-21.7	-8.4	1.6	-2.4	1.1	2.8	-1.8	-7.5	-10.5	18.9	-62.0	47.8	-25.2	-28.7	10.8	

FIG. 9. Correlation matrix of standard cosmological parameters with GDM parameters in the var-wc model when the PPS+Lens+BAO dataset combination was used with flat priors. The number in each matrix element indicates the value of the corresponding correlation coefficient, multiplied by a factor of 100. The color of each element also reflects the strength of the correlation, from dark blue (= -1) to dark red (= 1) through white (= 0).

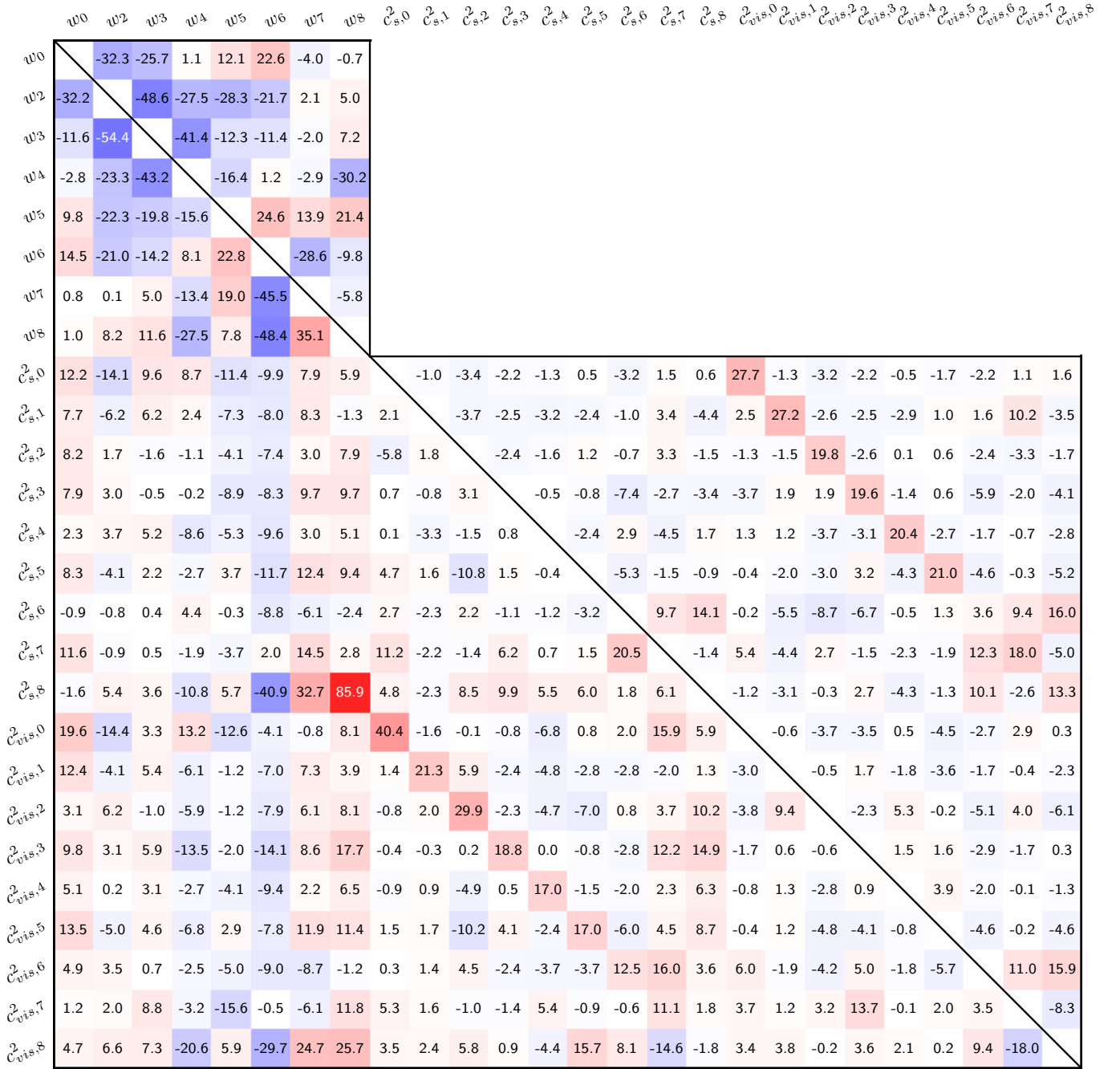


FIG. 10. Correlation matrix of GDM parameters for *var-wc* (lower triangle), *var-w* (upper triangle) and *var-c* (right triangle) when the PPS+Lens+BAO dataset combination with nonflat priors. The number in each matrix element indicates the value of the corresponding correlation coefficient, multiplied by a factor of 100. The color of each element also reflects the strength of the correlation, from dark blue (= -1) to dark red (= 1) through white (= 0).